



Numerical Simulations of a Quiet SuperSonic Technology (QueSST) Aircraft Preliminary Design

*David J. Friedlander, Christopher M. Heath, and Raymond S. Castner
Glenn Research Center, Cleveland, Ohio*

NASA STI Program . . . in Profile

Since its founding, NASA has been dedicated to the advancement of aeronautics and space science. The NASA Scientific and Technical Information (STI) Program plays a key part in helping NASA maintain this important role.

The NASA STI Program operates under the auspices of the Agency Chief Information Officer. It collects, organizes, provides for archiving, and disseminates NASA's STI. The NASA STI Program provides access to the NASA Technical Report Server—Registered (NTRS Reg) and NASA Technical Report Server—Public (NTRS) thus providing one of the largest collections of aeronautical and space science STI in the world. Results are published in both non-NASA channels and by NASA in the NASA STI Report Series, which includes the following report types:

- **TECHNICAL PUBLICATION.** Reports of completed research or a major significant phase of research that present the results of NASA programs and include extensive data or theoretical analysis. Includes compilations of significant scientific and technical data and information deemed to be of continuing reference value. NASA counter-part of peer-reviewed formal professional papers, but has less stringent limitations on manuscript length and extent of graphic presentations.
- **TECHNICAL MEMORANDUM.** Scientific and technical findings that are preliminary or of specialized interest, e.g., “quick-release” reports, working papers, and bibliographies that contain minimal annotation. Does not contain extensive analysis.
- **CONTRACTOR REPORT.** Scientific and technical findings by NASA-sponsored contractors and grantees.
- **CONFERENCE PUBLICATION.** Collected papers from scientific and technical conferences, symposia, seminars, or other meetings sponsored or co-sponsored by NASA.
- **SPECIAL PUBLICATION.** Scientific, technical, or historical information from NASA programs, projects, and missions, often concerned with subjects having substantial public interest.
- **TECHNICAL TRANSLATION.** English-language translations of foreign scientific and technical material pertinent to NASA's mission.

For more information about the NASA STI program, see the following:

- Access the NASA STI program home page at <http://www.sti.nasa.gov>
- E-mail your question to help@sti.nasa.gov
- Fax your question to the NASA STI Information Desk at 757-864-6500
- Telephone the NASA STI Information Desk at 757-864-9658
- Write to:
NASA STI Program
Mail Stop 148
NASA Langley Research Center
Hampton, VA 23681-2199



Numerical Simulations of a Quiet SuperSonic Technology (QueSST) Aircraft Preliminary Design

*David J. Friedlander, Christopher M. Heath, and Raymond S. Castner
Glenn Research Center, Cleveland, Ohio*

National Aeronautics and
Space Administration

Glenn Research Center
Cleveland, Ohio 44135

Acknowledgments

The authors would like to thank the NASA Advanced Air Vehicles Program, Commercial Supersonic Technology Project for funding and the NASA's High-End Computing Program for providing super-computing resources. The authors would also like to thank Mike Park for guidance on the grid adaptation process and Stefanie Hirt for providing statistics guidance and the Tecplot macro script used to create the total pressure recovery contour plots.

Trade names and trademarks are used in this report for identification only. Their usage does not constitute an official endorsement, either expressed or implied, by the National Aeronautics and Space Administration.

This work was sponsored by the Advanced Air Vehicle Program
at the NASA Glenn Research Center

Level of Review: This material has been technically reviewed by technical management.

Available from

NASA STI Program
Mail Stop 148
NASA Langley Research Center
Hampton, VA 23681-2199

National Technical Information Service
5285 Port Royal Road
Springfield, VA 22161
703-605-6000

This report is available in electronic form at <http://www.sti.nasa.gov/> and <http://ntrs.nasa.gov/>

Numerical Simulations of a Quiet SuperSonic Technology (QueSST) Aircraft Preliminary Design

David J. Friedlander, Christopher M. Heath, and Raymond S. Castner
National Aeronautics and Space Administration
Glenn Research Center
Cleveland, Ohio 44135

Abstract

Reynolds Averaged Navier-Stokes (RANS) simulations were performed on a Lockheed Martin Quiet SuperSonic Technology (QueSST) aircraft preliminary design to assess inlet performance. The FUN3D flow solver and its adjoint-based grid refinement capability were used for the simulations in hopes of determining internal “best practices” for predicting inlet performance on top-aft-mounted inlets. Several parameters were explored including tetrahedral versus pentahedral cells in/around the boundary-layer regions, an engine axis-aligned linear pressure sensor versus a pressure box objective as the grid adaptation metric, and the number of grid adaptation cycles performed. Additional simulations were performed on manually refined grids for comparison with the adjoint-based adapted grids. Results showed poor agreement in predicted inlet performance on the refined grids compared to experimental data. This was true regardless of whether the refinement was adjoint-based or manual, the cell type in/near the boundary-layer regions, or the grid adaptation metric used. In addition, the 40-probe total pressure recovery was shown to decrease asymptotically as the number of adaptation cycles was increased. Solutions on the unadapted grids generally had better agreement with experimental data than their refined grid counterparts.

Nomenclature

DPCP	Inlet circumferential distortion
DPRP	Inlet radial distortion
M	Mach number
m_2/m_0	Inlet mass flow rate ratio
p, p_t	Static and total pressure
$p_{t,2}/p_{t,\infty}$	Inlet total pressure recovery
u	Streamwise velocity
x, y, z	Cartesian coordinates
y^+	Nondimensional wall distance
α	Angle of attack
β	Sideslip angle
σ	Standard deviation
∞	Freestream

1.0 Introduction

Although there has not been a commercial supersonic flight since the retirement of the Concorde fleet in 2003, the aviation community has shown interest in bringing back commercial supersonic transports, with several companies already pursuing efforts (Refs. 1 to 3). These efforts are on-going despite the current ban on supersonic flight over U.S. territories due to the loudness of the sonic booms produced by aircraft flying at supersonic speeds (Ref. 4). NASA has taken an interest in paving the way for commercial supersonic transport aircraft in the United States (Ref. 5) and had gone as far as devoting one of the x-planes in the New Aviation Horizons initiative to demonstrating that an aircraft flying supersonically can generate a quiet sonic boom (Ref. 6). This low boom flight demonstrator aircraft was contracted out to Lockheed Martin by NASA to develop the aircraft through the preliminary design review (Ref. 7). While several incarnations of the aircraft were analyzed by both Lockheed Martin engineers and NASA researchers, the C607.1 version of the Quiet SuperSonic Technology (QueSST) aircraft was chosen for wind tunnel aerodynamic and propulsion tests in the NASA Glenn Research Center's (GRC's) 8- by 6-Supersonic Wind Tunnel (SWT) during the first half of 2017. This paper focuses on the Reynolds Averaged Navier-Stokes (RANS) computational fluid dynamic (CFD) simulations performed by the NASA GRC researchers that supported the propulsion wind tunnel test effort.

2.0 Geometry and Numerical Modeling

2.1 QueSST C607.1 Geometry

The QueSST aircraft preliminary design, shown in Figure 1, is a single engine aircraft, with the engine top-mounted at the aft-end of the fuselage. The inlet is an external compression diverter-less bump inlet that compresses the flow external of the inlet duct while diverting the boundary-layer flow away from the engine intake. The C607.1 version, shown in Figure 2 with features highlighted in Figure 3, has modified internal inlet contours with respect to its predecessors in order to improve inlet performance. The inlet itself has a throat area of 510 in.² and a subsonic diffuser length of 96 in. Vortex generators are situated approximately 10 inlet diameters upstream of the inlet in order to help mitigate boundary-layer flow from being ingested by the inlet. Approximately 15 inlet diameters upstream of the vortex generators is a camera fairing for housing an external camera system. The camera system is required to help aid the pilot with take-offs and landings due to the minimal visibility from the cockpit. The presented simulations use a 9.5 percent scaled version of the C607.1 aircraft, which is consistent with the scale of the wind tunnel model used in the 8×6 SWT aerodynamic and propulsion tests.



Figure 1.—Artist's concept of the Lockheed Martin QueSST aircraft preliminary design (Ref. 5).

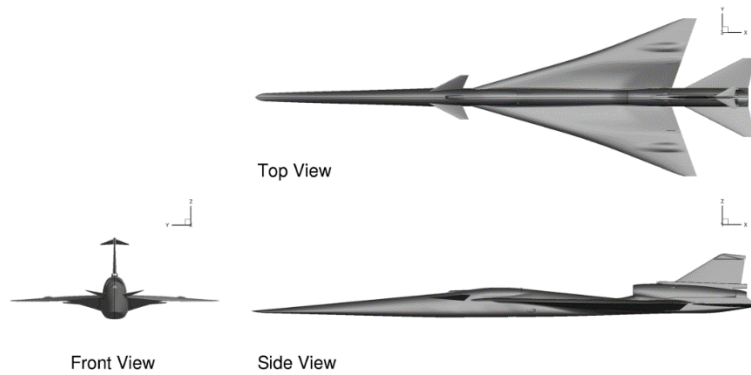


Figure 2.—QueSST C607.1 aircraft preliminary design.

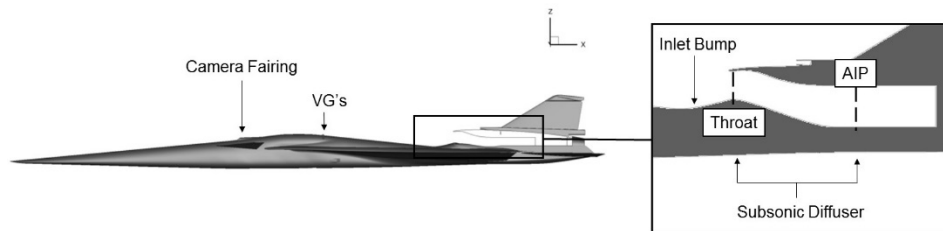


Figure 3.—QueSST C607.1 aircraft features, including the aerodynamic interface plane (AIP).

2.2 Flow Solver

NASA’s FUN3D (Ref. 8) code was used for all simulations. FUN3D is a node-based production level code developed and maintained at the NASA Langley Research Center. It can solve 2D/3D Euler and RANS equations for incompressible and compressible flows on unstructured grids. The FUN3D flow solver was chosen for two main reasons: (1) it can handle complex geometries represented by unstructured grids and (2) it has the capability to perform adjoint-based grid adaptation. The adjoint-based grid adaption uses the refine/one library (Ref. 9), which requires “freezing” all boundary-layer (BL) cells within a user-specified distance from no-slip walls. FUN3D’s adjoint-based grid adaptation capability has been used extensively with external flow applications including complex nozzle plumes (Refs. 9 to 11) and sonic boom predictions (Ref. 12), as well as internal flow applications such as s-ducts (Ref. 13). The adjoint-based grid adaptation works by reducing the grid spatial discretization error with respect to a specified flow field metric by leveraging flow solution sensitivities. For the presented simulations, the pressure within the inlet duct was chosen as the flow field metric for adaptation.

2.3 Grid Adaptation Parameters

In order to develop internal “best practices” for capturing top-aft-mounted inlet performance, three parameters were chosen to explore their sensitivities on the predicted inlet performance. These included the cell type in/near the boundary-layer, the grid adaptation metric, and the number of grid adaptation cycles. The cell type looked at using tetrahedrals or pentahedrals (i.e., prisms and pyramids) in and around the boundary-layer regions. The two grid adaptation metrics that were explored were an engine axis-aligned linear pressure sensor and a pressure box objective. The linear pressure sensor objective works by minimizing the discretization error around a linear pressure “sensor” while the pressure box objective works by computing the RMS values of pressure. Each objective is only active within a user specified region of the flow field domain. Finally, the number of grid adaptation cycles was varied from 8 to 16 cycles. Table 1 summarizes the combinations of the parameters that were studied.

TABLE 1.—GRID ADAPTATION CASES

Case #	BL cell type	Adaptation metric	Adaptation cycles
1	Tetrahedral	NA	0
2	Tetrahedral	Linear pressure sensor	8
3	Pentahedral	NA	0
4	Pentahedral	Pressure box	8
5	Tetrahedral	Pressure box	^a 8
6	Tetrahedral	Pressure box	^a 16
7	Pentahedral	Pressure box	^a 8
8	Pentahedral	Pressure box	^a 16

^aReduced number of additional nodes/adaptation cycle.

TABLE 2.—SET POINT CONDITIONS.

Reading #	Mach number	α , degree	β , degree
1755	1.46	2.0	0.0
1771	1.35	3.0	0.0
2033	0.30	3.0	0.0

2.4 Initial and Manually Refined Grids

An unstructured surface grid was generated using the Pointwise (Ref. 14) grid generation software while three different initial volume grids were generated using the AFLR3 (Ref. 15) code. AFLR3 is a research code developed at Mississippi State University that generates unstructured tetrahedral/pentahedral volume grids via the Advancing-Front/Local Reconstruction method (Refs. 16 and 17). The three initial volume grids were differentiated as follows; grid #1 consisted of all tetrahedral cells (referred to as the tetrahedral boundary-layer grid), grid #2 contained a mix of tetrahedral and pentahedral cells (referred to as the pentahedral boundary-layer grid), and grid #3 was a smoothed version of grid #2 (referred to as the pentahedral boundary-layer smooth grid or case number 3A). Viscous spacing was such that the y^+ value was less than 0.2. Nodal count for all initial grids was 33.4 million. Due to symmetry, only half of the aircraft was modeled.

In addition, two manually refined grids, one based off of grid #1 and the other based off of grid #2, were developed following the same process as the initial grids for comparison with the adapted grids, and are referred to as case numbers 9 and 10, respectively. Refinement took the form of uniformly increasing the nodal count on the surface grid connectors by a factor of 1.5 and decreasing the initial spacing off the viscous surfaces by a factor of 1.5. This resulted in volume grids with 92.3 million nodes for the tetrahedral boundary-layer based grid and 91.8 million nodes for the pentahedral boundary-layer based grid.

2.5 Flow Conditions

Three different experimental set points were chosen for the simulations, with details outlined in Table 2. Most of the simulations focused on the set point condition referred to as Reading 1755, which at $M_\infty = 1.46$ was slightly higher than the aircraft's designed freestream cruise condition of $M_\infty = 1.42$. Additionally, a lower supersonic point of $M_\infty = 1.35$ (Reading 1771) and a low subsonic point of $M_\infty = 0.30$ (Reading 2033) were chosen for additional comparisons.

2.6 Boundary Conditions, Initial Solutions, and Turbulence Modeling

A combination of freestream and farfield boundary conditions were applied to the outer boundaries of the computational domain, shown in Figure 4 for the supersonic flow cases and Figure 5 for the subsonic flow case. An extrapolation boundary condition was applied to the outflow boundary for the supersonic flow cases while a farfield boundary condition was applied for the subsonic flow case. Mass flow through the inlet was set indirectly by specifying the inlet exit plane Mach number, which in turn set the back pressure within the inlet duct. Setting the mass flow through the inlet in this manner was in lieu of modeling the

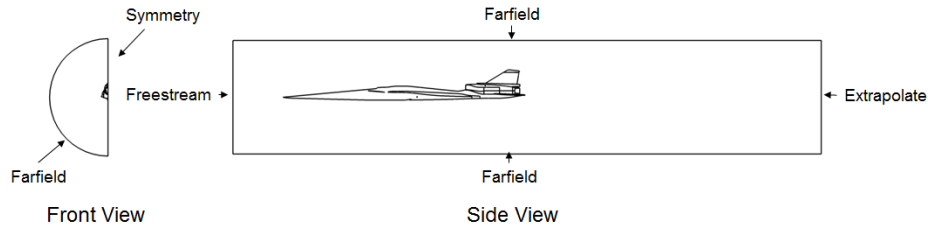


Figure 4.—Boundary conditions for supersonic flow conditions.

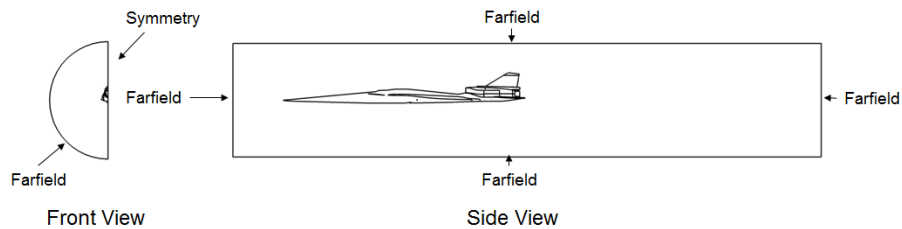


Figure 5.—Boundary conditions for subsonic flow condition.

mass flow plug that was used in the experiment. Flow through the nozzle was set by imposing a subsonic inflow boundary condition at the nozzle inflow plane, where the total pressure and total temperature ratios were specified. Initial solutions were set to uniform flow at the freestream conditions with the exception of the inlet duct, which was initialized at a subsonic uniform flow. All simulations used the Spalart-Allmaras turbulence model (Ref. 18).

3.0 Results

The presented results will mostly focus on the solutions along the aircraft centerline. While the inlet was the main area of interest, two additional stations upstream of the inlet were chosen for comparison with experimental data: the area around the camera fairing and the area at the inlet bump. Figure 6 shows all of the areas of interest while Figure 7 shows the experiment pressure tap locations at the camera fairing and inlet bump regions. For reference, the nose of the aircraft is at axial station $x = 2.419$ in., which is consistent with the aircraft model run in the experiment. In addition, the inlet mass flow rate ratio was defined as the ratio of the mass flow rate at the aerodynamic interface plane (AIP), m_2 , to the theoretical capture mass flow rate, m_0 . The capture mass flow rate utilized the inlet throat area as the capture area, which does not account for the pre-compression surface of the inlet bump diverter. Thus, some of the mass flow rate ratios reported in this paper exceed 1.00.

3.1 Statistical Approach

Paired t-tests were performed in order to help quantify the comparisons between the CFD solutions to themselves and the experimental data. By definition, the paired t-tests were performed on the differences between the data being compared and not the absolute values themselves. For example, if a paired t-test were to be performed on data derived from CFD simulations and an experiment, shown in Table 3, the paired t-test would be performed on the differences between the two data sets, i.e., the fourth column of Table 3. Due to the limited number of CFD simulation data points available, the statistical comparisons presented in this paper utilized only 4-8 points per comparison. While this is not ideal, it is the hope of the authors that the presented framework can be utilized for future CFD simulation comparisons.

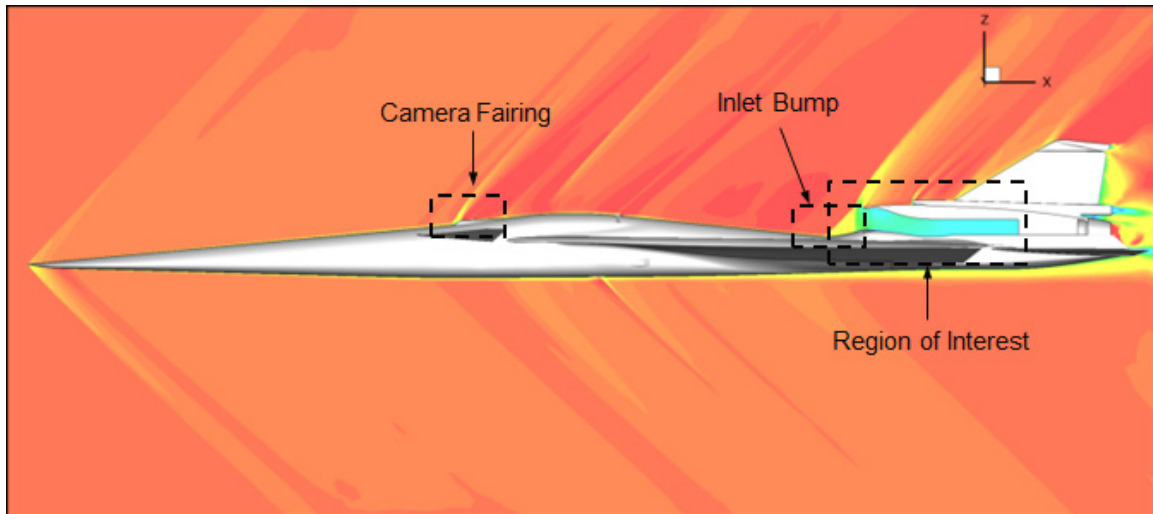


Figure 6.—Areas of interest along the aircraft centerline.

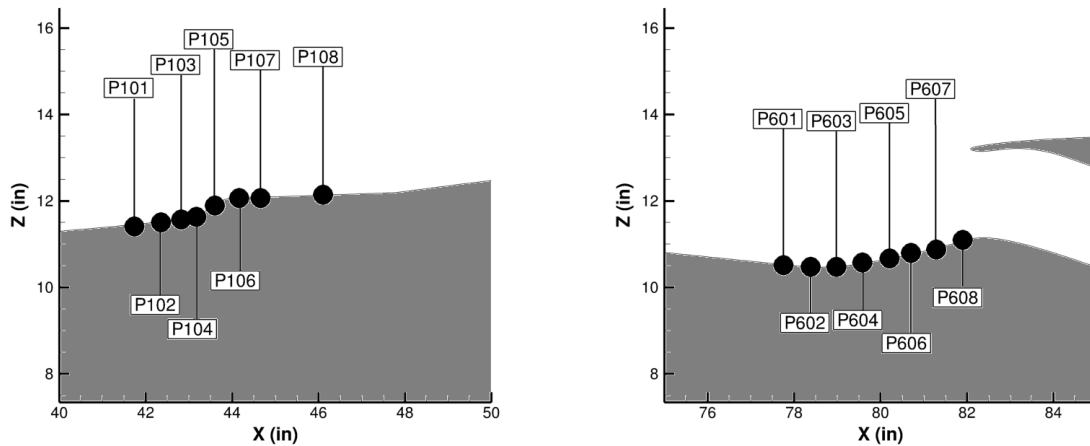


Figure 7.—Experiment pressure tap locations along the aircraft centerline at the camera fairing region (left) and inlet bump region (right).

TABLE 3.—EXAMPLE PRESSURE DATA (AS A FUNCTION OF THE INLET MASS FLOW RATE RATIO) AT ONE OF THE CAMERA FAIRING PRESSURE TAP LOCATIONS

m_2/m_0	CFD, psf	Experiment, psf	CFD—Experiment, psf	Average, psf	2σ , psf
0.84	809.747	784.709	25.038	25.484	1.951
0.92	809.747	783.097	26.650		
0.99	809.747	783.903	25.844		
1.03	809.747	785.343	24.404		

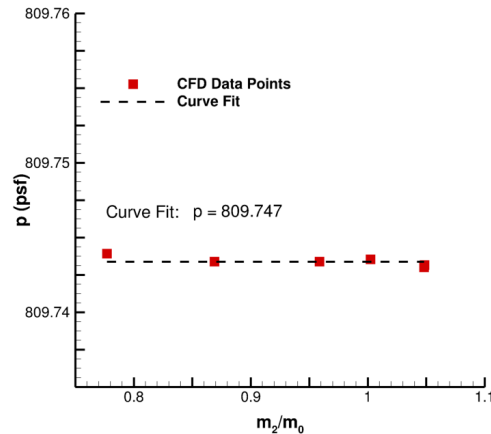


Figure 8.—Example CFD curve fit at one of the camera fairing pressure tap locations.

Although the CFD simulations were run at the experimental freestream conditions, the CFD simulations were not necessarily run at the same inlet mass flow rate ratios as the experiment, therefore, curve fits were applied to the CFD data for a one-to-one comparison with the experimental data; see Appendix A for the inlet mass flow rate ratios that the CFD simulations were run at. The curve fits were generated using a least-squares error method to fit a 5th-order or lower polynomial to the CFD data as a function of the inlet mass flow rate ratio, with an example curve fit shown in Figure 8. Note that the order of the polynomials were kept to at most one more than half the number of points available. For example, if the number of points available was eight, then the highest order polynomial curve fit considered was fifth order. CFD data with curve fits with an R-squared value less than 0.8 were omitted from the statistical comparisons and the curve fits were used only for interpolation. See Appendix B for all the curve fit and R-squared values for the curve fits used in the statistical comparisons. Figures that utilize the curve fits have an asterisk at the end of each figure caption. See Appendix C for all the average and two times the standard deviation values from the performed t-tests. The reader is cautioned that there is a difference between being statistically the same/different and being the same/different from an engineering perspective. For example, two data sets might be close enough that from an engineering perspective they are the same, but statistically they are different due to the standard deviations being smaller than the average difference between the two data sets. This will come into play in the following subsections.

3.2 Cell Type and Grid Adaptation Metric

Figure 9 shows the inlet Mach number contour on the unadapted tetrahedral boundary-layer grid (case #1) at the Reading 1755 conditions ($M_\infty = 1.46$, $\alpha = 2.0^\circ$) for an inlet mass flow ratio of 0.96. It can be seen that FUN3D predicts a small separation region within the subsonic diffuser. This separation region is an artifact of the shockwave boundary-layer interaction occurring upstream in the inlet bump region and therefore is sensitive to how well the CFD code can predict the shockwave strength and location. Further, this separation region is shown to be greatly exaggerated after 8 adaptation cycles (case #2), shown in Figure 10, when using the engine axis-aligned linear pressure sensor. Note that during the adaptation process, the boundary-layer cells were “frozen” below a y^+ of ~ 300 in order to permit a smooth transition from the viscous layers. Figure 11 shows the inlet Mach number contour on the unadapted pentahedral boundary-layer grid (case #3) at the Reading 1755 conditions for an inlet mass flow ratio of 0.95. Just like on the unadapted tetrahedral grid, FUN3D predicts a small separation region within the subsonic diffuser. This too is greatly exaggerated after 8 adaptation cycles (case #4) using the pressure box objective within the inlet subsonic diffuser, shown in Figure 12. It should be noted that unlike the 8 adaptation cycle tetrahedral boundary-layer grid, the 8 adaptation cycle pentahedral boundary-layer grid has an abrupt transition from the viscous regions. This is because FUN3D’s adjoint-based grid adaptation refine/one library does not adapt pentahedral cells, and thus these cells were the

only cells that were “frozen” during the adaptation process. In order to try to mitigate this abrupt transition, the smoothed version of the unadapted pentahedral boundary-layer grid (case #3A) was run at the Reading 1755 conditions, with the Mach number contour for an inlet mass flow rate ratio of 0.95 shown in Figure 13. In this case, FUN3D predicts a much larger separation compared to the previous unadapted grids, although it is still smaller than the ones predicted by the adapted grids. It was decided not to try adapting the pentahedral boundary-layer smooth grid as the previous results showed that adapting the grid would only increase the size of the separation region.

While comparing aircraft centerline Mach number contours is reasonable for qualitative CFD solution comparisons, it does not answer the question of how well each solution is correctly predicting the flow field, let alone predicting inlet performance. To help answer these questions, the static pressure profiles at the camera fairing and inlet bump regions were plotted at various inlet mass flow rate ratios. Some of these are shown in Figure 14 and Figure 15 for the camera fairing region and Figure 16 to Figure 18 for the inlet bump region. The camera fairing region figures show that the pressure measurements at this location are insensitive to the inlet mass flow rate ratio, with the exception of the fourth upstream pressure station ($x = 43.2$) on the unadapted tetrahedral boundary-layer grid. The insensitivity is to be expected as the inlet is well downstream of the camera fairing location. Note, the CFD solutions on the pentahedral boundary-layer based grids (cases #3, #4, and #3A) were not shown in the camera fairing location figures as the trends were identical to the CFD solutions on the tetrahedral boundary-layer based grids (cases #1 and #2). The inlet bump region figures show that the pressure profiles are insensitive to the inlet mass flow rate ratio only to about $x = 79.0$ in. to $x = 80.7$ in., depending on the grid, at which point, the pressure measurements tend to decrease as the mass flow rate ratio is increased. To further compare the CFD solutions and the experimental data, the static pressure profiles at the camera fairing and inlet bump at an inlet mass flow rate ratio of 0.95 were plotted, as shown in Figure 19. Note that the uncertainty in the experiment pressure data is ± 2.16 psf. It can be seen that the solutions from the pentahedral boundary-layer grids (cases #3, #4, and #3A) matched the experimental data better at the camera fairing compared to their tetrahedral boundary-layer grid (cases #1 and #2) counterparts. This trend holds true downstream at the inlet bump as all CFD solutions tend to agree well with the experimental data, with the exception of the 8 adaptation cycle tetrahedral boundary-layer grid.

In terms of inlet performance, the 40-probe average total pressure recovery, shown in Figure 20, was better predicted on the unadapted grids compared to their adapted counterparts. To give a qualitative idea of inlet distortion, the computed 40-probe total pressure recovery contours at the AIP are shown in Figure 21 to Figure 23. These show that the size of the lower total pressure recovery region in the bottom portion of the inlet increased in the adapted cases compared to the unadapted cases. This trend is related to the increase in the separation region shown in the Mach number contour plots. Unlike the aircraft centerline Mach number contour plots, experimental data was available at the AIP. It is shown that the CFD first under predicts and then over predicts the size of the lower total pressure recovery region. To quantify the inlet distortion, ARP 1420 distortion parameters (Ref. 19) were computed and are shown in Figure 24 to Figure 27. Unlike the total pressure recovery, qualitatively the inlet distortion was not well predicted by any of the CFD solutions. However, only the circumferential inlet distortion computed on the unadapted tetrahedral boundary-layer and unadapted pentahedral boundary-layer smooth grids were statistically the same as the experimental data at the 95 percent confidence level. Also, the circumferential inlet distortion computed on the unadapted tetrahedral boundary-layer grid and the unadapted pentahedral boundary-layer smooth grid were statistically the same at the 95 percent confidence level and the circumferential inlet distortion computed on the adapted grids were statistically the same at the 95 percent confidence level. None of the radial distortions computed on the grids were statistically the same as the experiment at the 95 percent confidence level, while the following radial distortions computed on the following grids were statistically the same at the 95 percent confidence level: (1) unadapted tetrahedral boundary-layer grid and unadapted pentahedral boundary-layer grid, (2) 8 adaptation cycle tetrahedral boundary-layer grid and unadapted pentahedral boundary-layer grid, (3) 8 adaptation cycle tetrahedral boundary-layer grid and unadapted tetrahedral boundary-layer grid, and (4) 8 adaptation cycle tetrahedral boundary-layer grid and unadapted pentahedral boundary-layer smooth grid.

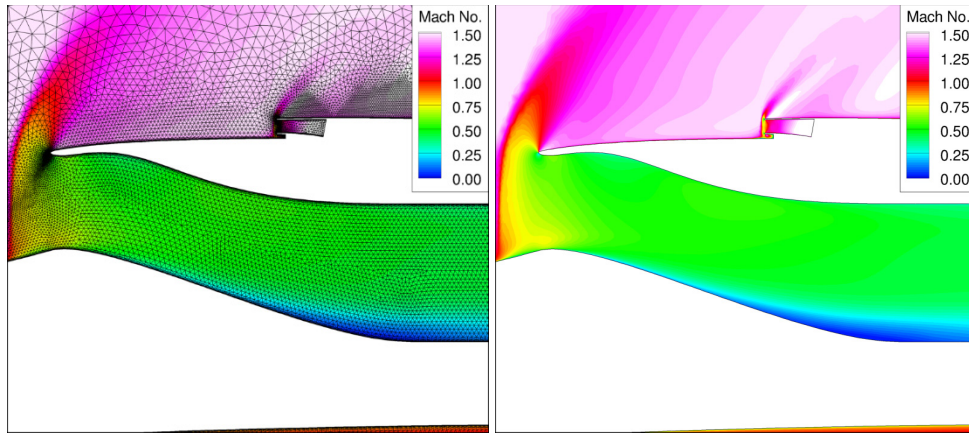


Figure 9.—Mach number contours for the unadapted tetrahedral boundary-layer grid (case #1), $m_2/m_0 = 0.96$.

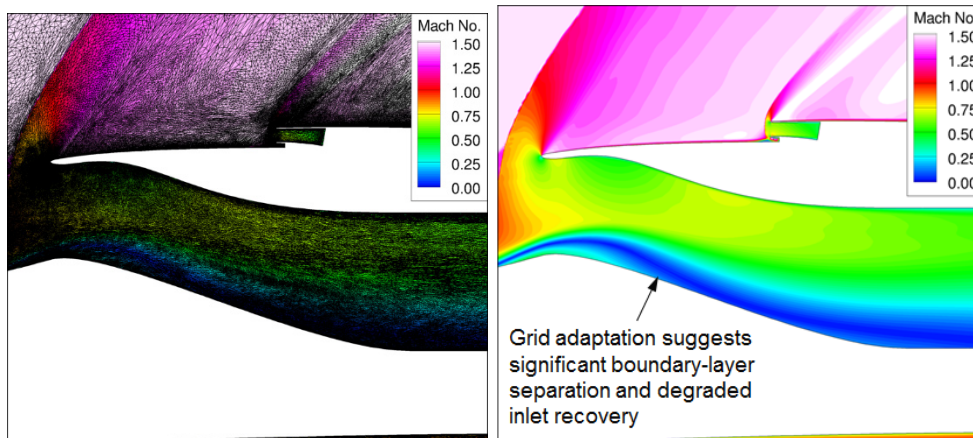


Figure 10.—Mach number contours for the 8 adaptation cycle tetrahedral boundary-layer grid (case #2), $m_2/m_0 = 0.93$.

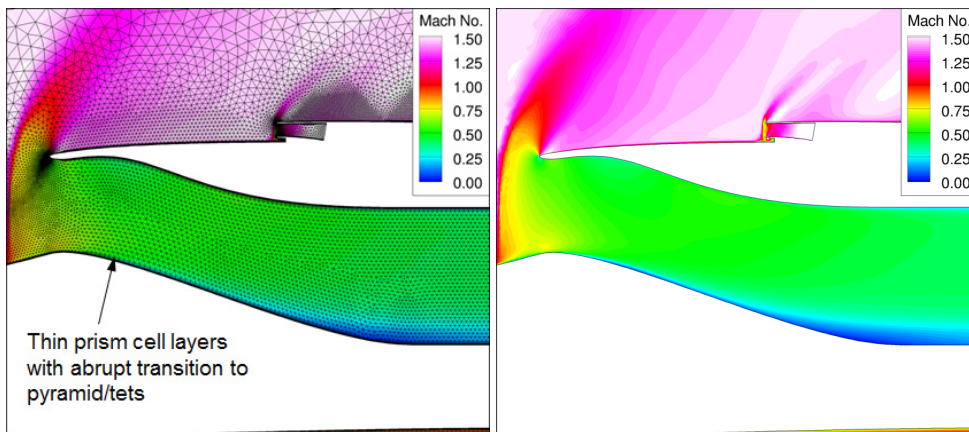


Figure 11.—Mach number contours for the unadapted pentahedral boundary-layer grid (case #3), $m_2/m_0 = 0.95$.

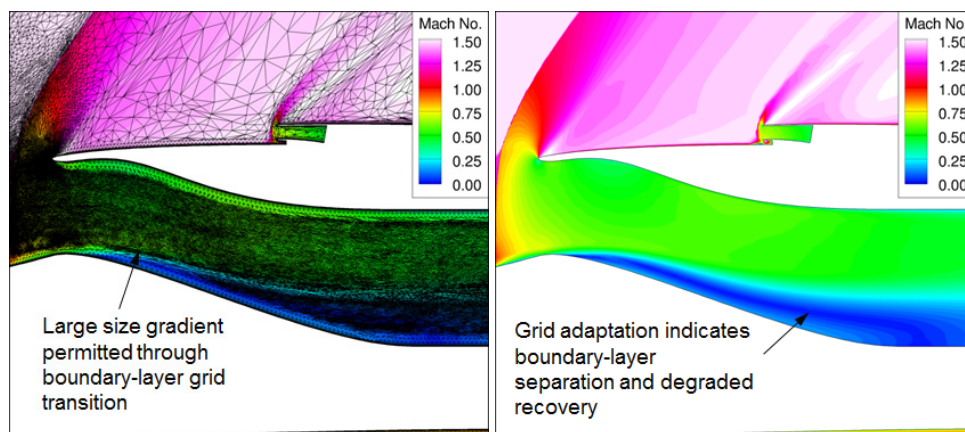


Figure 12.—Mach number contours for the 8 adaptation cycle pentahedral boundary-layer grid (case #4), $m_2/m_0 = 0.94$.

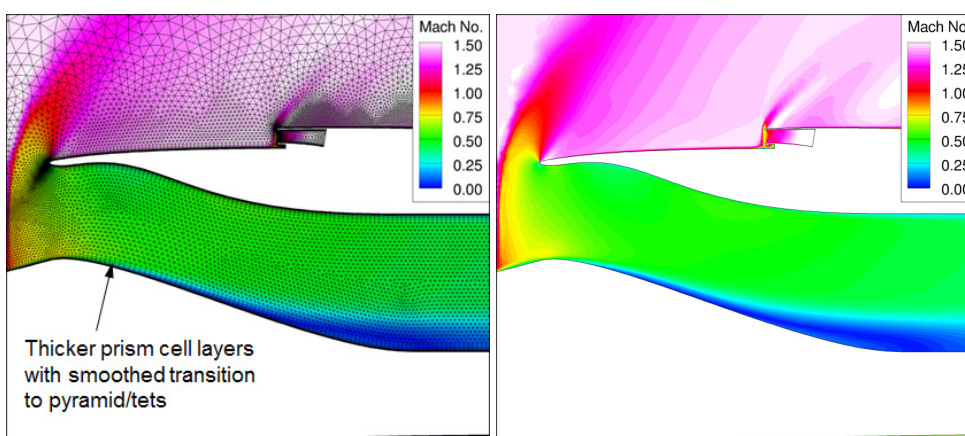


Figure 13.—Mach number contours for the unadapted pentahedral boundary-layer smooth grid (case #3A), $m_2/m_0 = 0.95$.

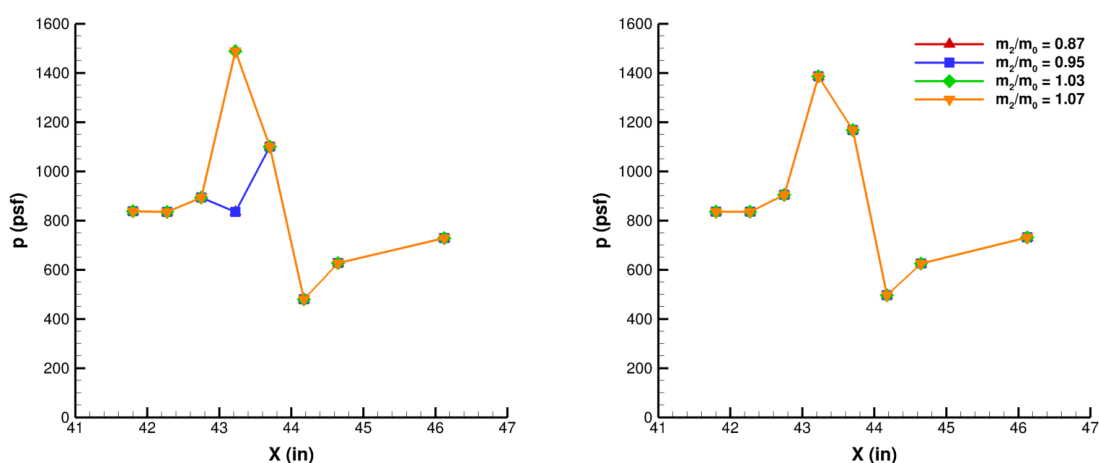


Figure 14.—Static pressure profiles along the camera fairing for the unadapted (case #1) (left) and 8 adaptation cycle (case #2) (right) tetrahedral boundary-layer grids for $M_\infty = 1.46$, $\alpha = 2.0^\circ$.

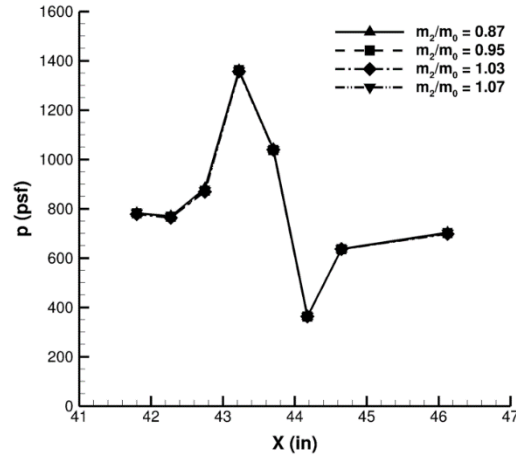


Figure 15.—Static pressure profiles along the camera fairing for the experiment at $M_\infty = 1.46$, $\alpha = 2.0^\circ$.

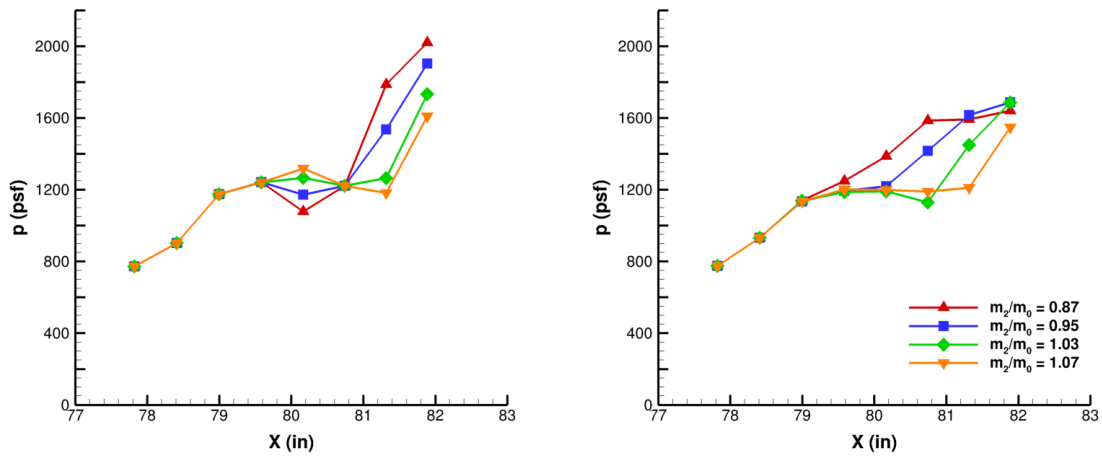


Figure 16.—Static pressure profiles along the inlet bump for the unadapted (case #1) (left) and 8 adaptation cycle (case #2) (right) tetrahedral boundary-layer grids for $M_\infty = 1.46$, $\alpha = 2.0^\circ$.*

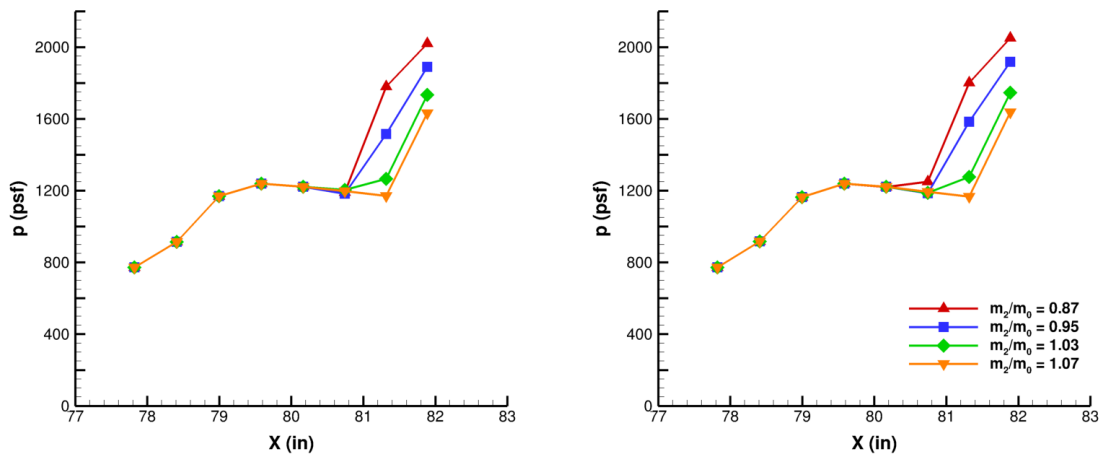


Figure 17.—Static pressure profiles along the inlet bump for the unadapted (case #3) (left) and 8 adaptation cycle (case #4) (right) pentahedral boundary-layer grids for $M_\infty = 1.46$, $\alpha = 2.0^\circ$.*

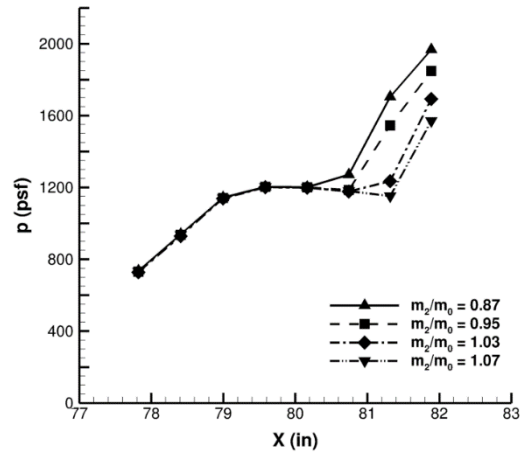


Figure 18.—Static pressure profiles along the inlet bump for the experiment at $M_\infty = 1.46$, $\alpha = 2.0^\circ$.

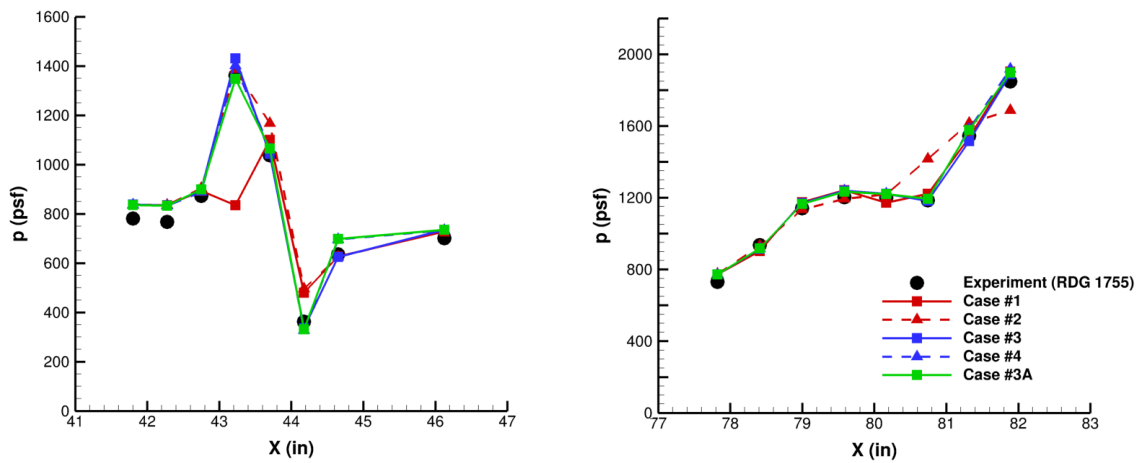


Figure 19.—Static pressure profiles along the camera fairing (left) and inlet bump (right) for $M_\infty = 1.46$, $\alpha = 2.0^\circ$, $m_2/m_0 = 0.95$.*

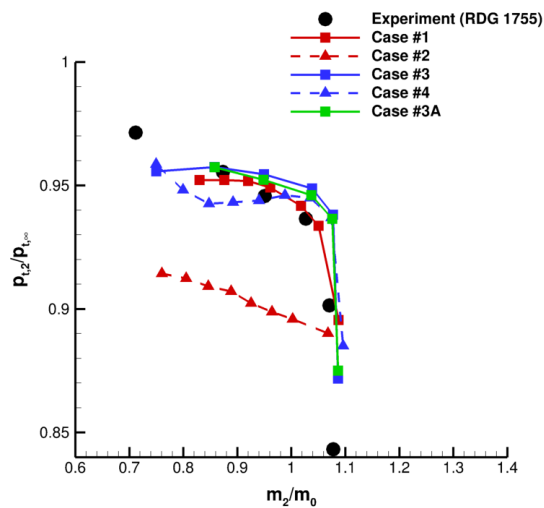


Figure 20.—The 40-probe total pressure recovery plot for $M_\infty = 1.46$, $\alpha = 2.0^\circ$.

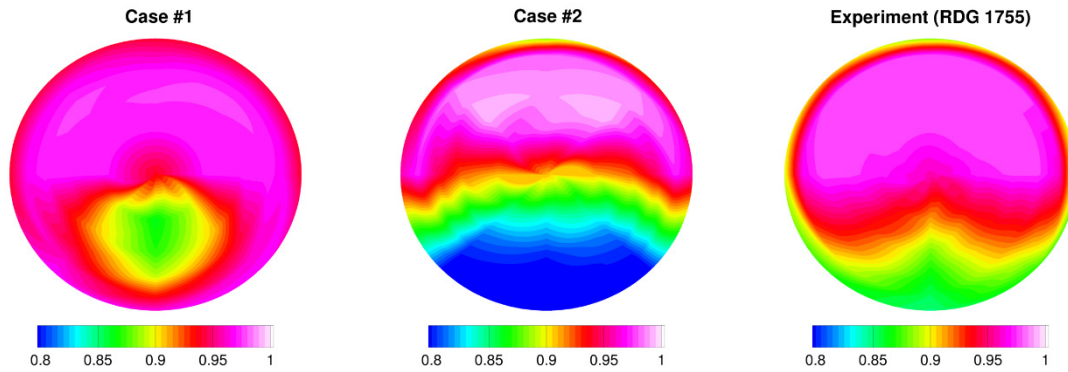


Figure 21.—The 40-probe total pressure recovery contours for the unadapted (left) and 8 adaptation cycle (middle) tetrahedral boundary-layer grid compared to the experiment (right) at $M_\infty = 1.46$, $\alpha = 2.0^\circ$.

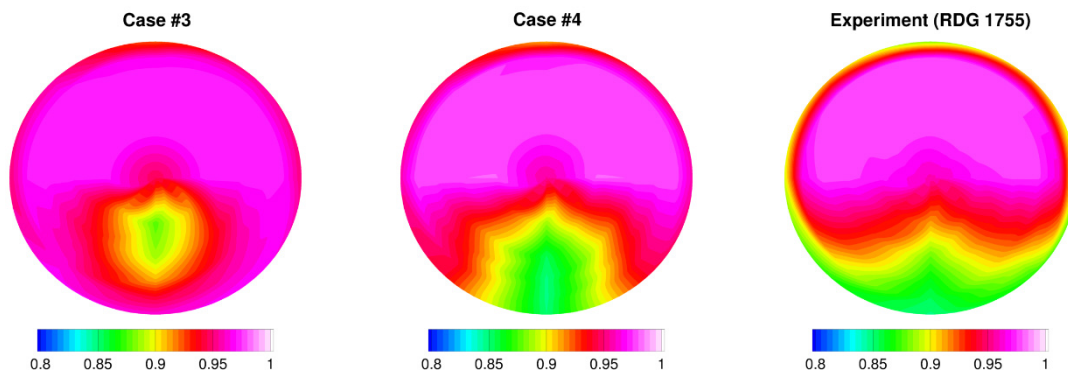


Figure 22.—The 40-probe total pressure recovery contours for the unadapted (left) and 8 adaptation cycle (middle) pentahedral boundary-layer grid compared to the experiment (right) at $M_\infty = 1.46$, $\alpha = 2.0^\circ$.

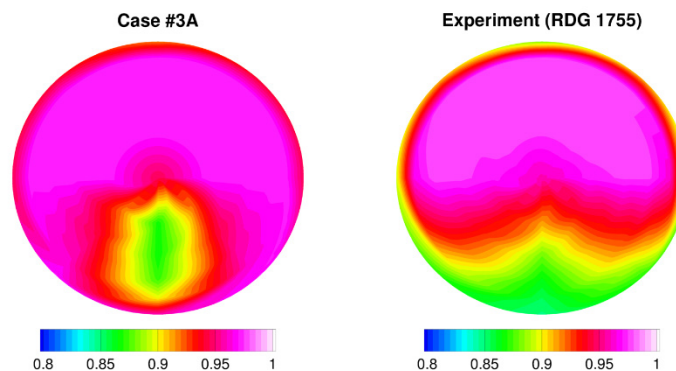


Figure 23.—The 40-probe total pressure recovery contours for the unadapted pentahedral boundary-layer smooth grid (left) and the experiment (right) at $M_\infty = 1.46$, $\alpha = 2.0^\circ$.

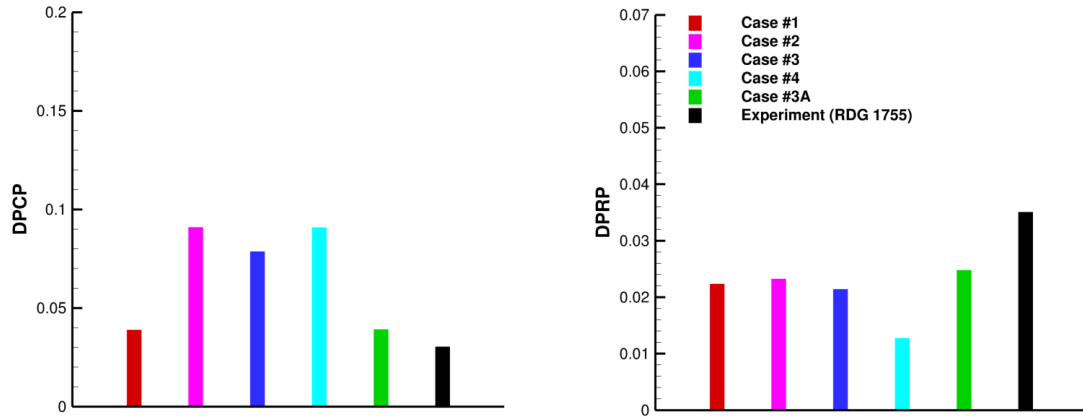


Figure 24.—Inlet circumferential distortion (left) and radial distortion (right) for $M_\infty = 1.46$, $\alpha = 2.0^\circ$, $m_2/m_0 = 0.87$.*

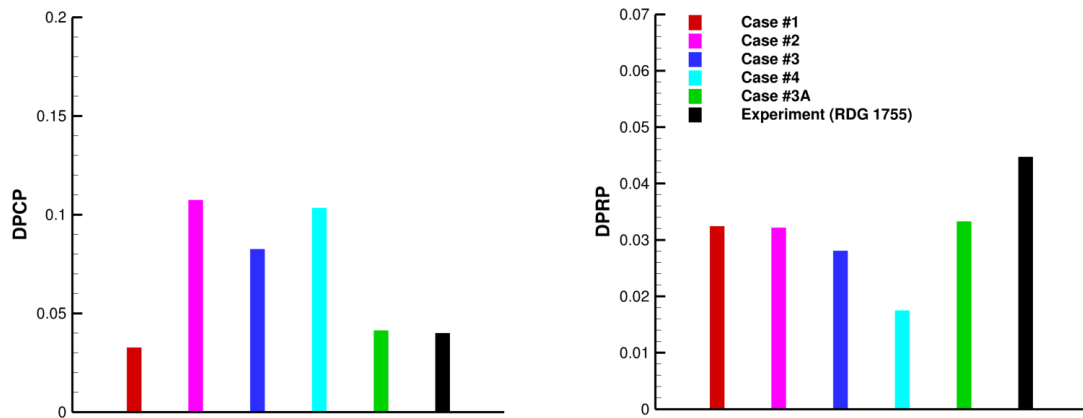


Figure 25.—Inlet circumferential distortion (left) and radial distortion (right) for $M_\infty = 1.46$, $\alpha = 2.0^\circ$, $m_2/m_0 = 0.95$.*

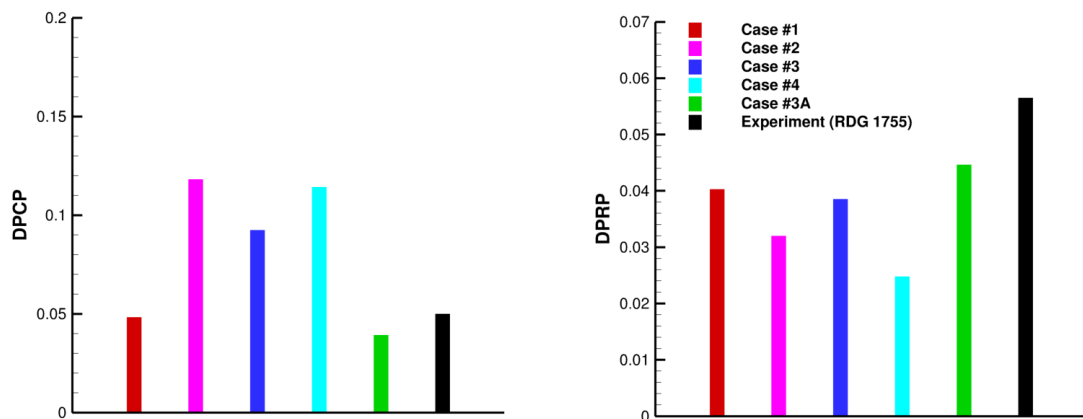


Figure 26.—Inlet circumferential distortion (left) and radial distortion (right) for $M_\infty = 1.46$, $\alpha = 2.0^\circ$, $m_2/m_0 = 1.03$.*

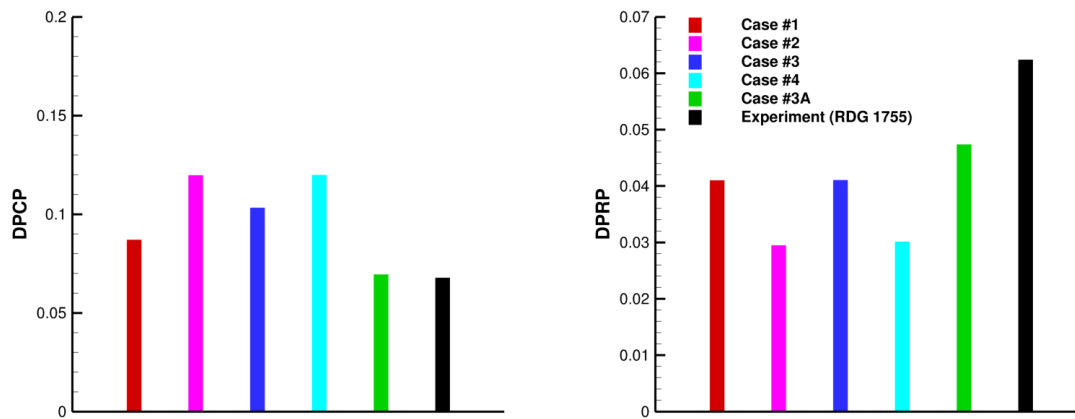


Figure 27.—Inlet circumferential distortion (left) and radial distortion (right) for $M_\infty = 1.46$, $\alpha = 2.0^\circ$, $m_2/m_0 = 1.07$.*

3.3 Number of Adaptation Cycles

While the number of adaptation cycles was increased from 8 to 16 for this sub-study, it should be noted that the target number of nodes added per adaptation cycle was decreased from 1×10^6 to 2×10^5 in order to reduce the grid size of the 16 adaptation cycle grids. Thus the 8 adaptation cycle grids presented in this subsection had approximately 25 to 54 percent fewer nodes compared to their counterparts in the previous subsection. Figure 28 and Figure 29 show the aircraft centerline Mach number contours for the 8 and 16 adaptation cycle tetrahedral boundary-layer grids (cases #5 and #6) at the Reading 1755 conditions ($M_\infty = 1.46$, $\alpha = 2.0^\circ$) while Figure 30 and Figure 31 show the aircraft centerline Mach number contours for the 8 and 16 adaptation cycle pentahedral boundary-layer grids (cases #7 and #8) at the Reading 1755 conditions. These figures show that there is very little difference in the flow field between 8 and 16 adaptation cycles. Also, they predict a large separation region in the subsonic diffuser, which is consistent with the separation regions predicted on the adapted grids (cases #2 and #4) shown in Figure 10 and Figure 12.

Figure 32 shows static pressure profiles at the camera fairing and the inlet bump at the Reading 1755 conditions for the unadapted (cases #1 and #3), 8 adaptation cycle (cases #5 and #7), and 16 adaptation cycle (cases #6 and #8) tetrahedral and pentahedral boundary-layer grids. The pressure profiles at the camera fairing generally agree with each other. Figure 32 also shows that the pressure profiles at the inlet bump generally agree with each other with the exception of the second to last pressure station ($x = 81.3$ in.).

In terms of the 40-probe average total pressure recovery, shown in Figure 33, both the pentahedral boundary-layer and tetrahedral boundary-layer grids (cases #3, #7, #8, #1, #5, #6) showed asymptotically decreasing total pressure recovery as the number of adaptation cycles was increased. This was more pronounced on the tetrahedral boundary-layer grids (cases #1, #5, and #6) than the pentahedral boundary-layer grids (cases #3, #7, and #8). The trend that the 40-probe average total pressure recovery asymptotically decreased as the number of adaptation cycles increased suggests that while adjoint-based grid adaptation will converge to a value for the 40-probe average total pressure recovery, that value will most likely not be the same value as that provided by experimental data. Further insight can be gained by looking at the computed AIP 40-probe total pressure recovery contour plots, shown in Figure 34 for the tetrahedral boundary-layer grids (cases #5 and #6) and Figure 35 for the pentahedral boundary-layer grids (cases #7 and #8). It can be seen that the total pressure recovery does not change significantly between 8 and 16 adaptation cycles and the region of lower total pressure recovery in the bottom portion of the inlet is over predicted. This is consistent with what was seen in the adapted grid solutions (cases #1, #2, #3, and #4) in Figure 21 and Figure 22.

Although using the adjoint-based solver in FUN3D resulted in poor agreement with the experimental data for these cases, the adjoint solver itself might not be the issue. In FUN3D, error estimates are computed after each adaptation cycle using the Venditti error estimate (Ref. 20). The computation of this error estimate, called the remaining adaptation error, is summarized in Equation (1).

$$\text{Remaining Adaptation Error} = \left(\left[\text{Flow Residual on Embedded Mesh} \right] \times \left[\text{Adjoint Interpolation Error} \right] \right) + \left(\left[\text{Adjoint Residual on Embedded Mesh} \right] \times \left[\text{Flow Interpolation Error} \right] \right) \quad (1)$$

Examining the remaining adaptation error for the pentahedral boundary-layer grid in Figure 36 shows that the remaining adaptation error is actually increasing over the course of the first 5 adaptation cycles and then steadies out to a relatively high value (on the order of 10^3). This is despite the fact that the flow residuals over the course of each adaptation cycle are shown to level out. Figure 36 also shows an example of the flow residuals during the 3rd adaptation cycle. Similar trends in the flow residuals were seen during the other adaptation cycles and the remaining adaptation error followed a similar trend for the tetrahedral boundary-layer grid. A possible reason for the lack of convergence of the remaining adaptation error is that the error estimation is using noisy data. The noisy data is most likely due to poor convergence of the flow equations, which in turn is due to numerical instability or physical unsteadiness of the flow field.

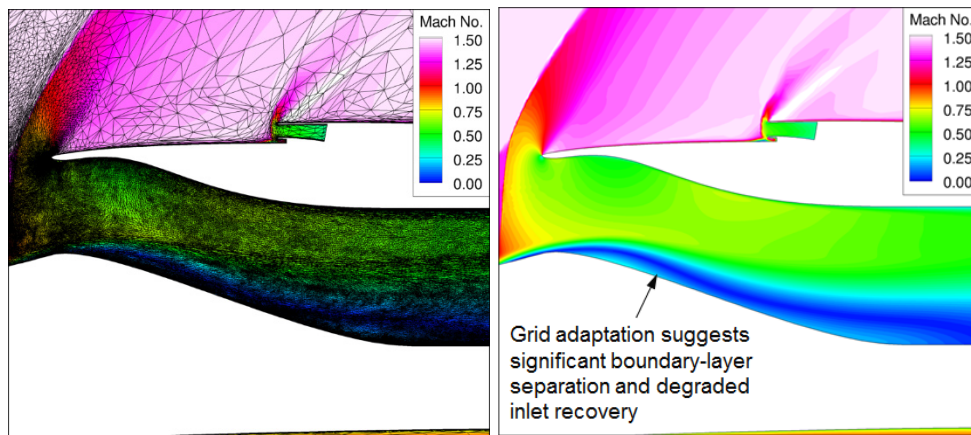


Figure 28.—Mach number contours for the 8 adaptation cycle tetrahedral boundary-layer grid (case #5), $m_2/m_0 = 0.97$.

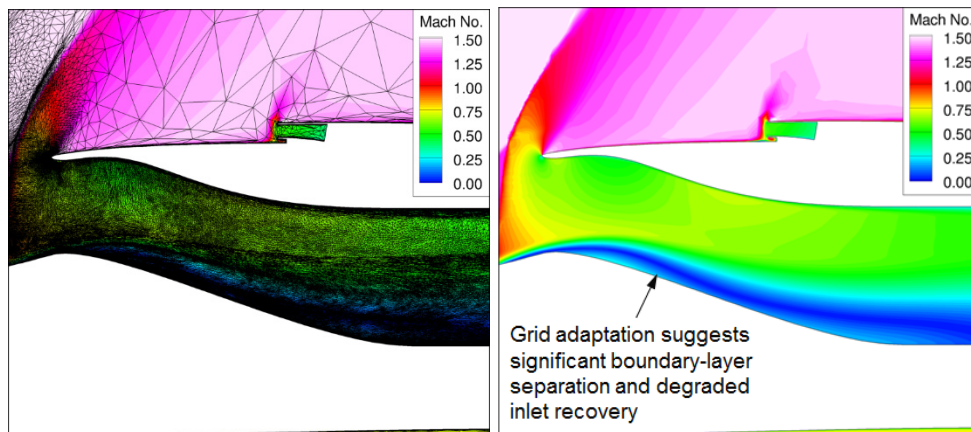


Figure 29.—Mach number contours for the 16 adaptation cycle tetrahedral boundary-layer grid (case #6), $m_2/m_0 = 0.97$.

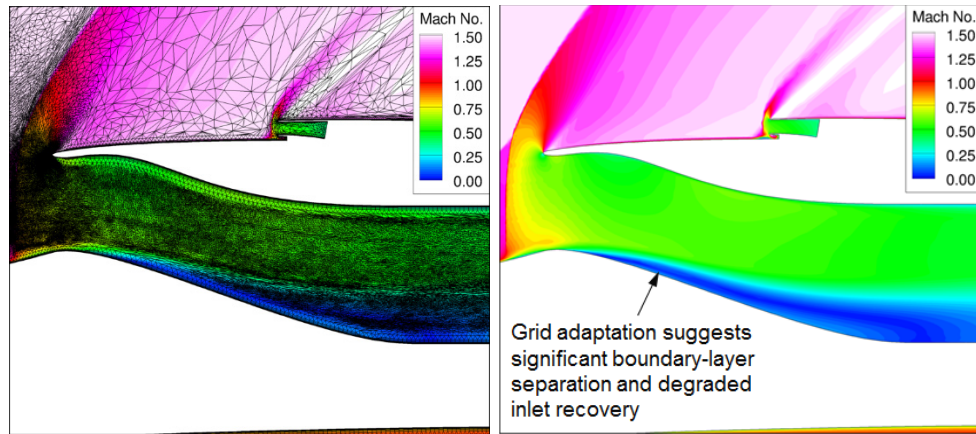


Figure 30.—Mach number contours for the 8 adaptation cycle pentahedral boundary-layer grid (case #7), $m_2/m_0 = 0.99$.

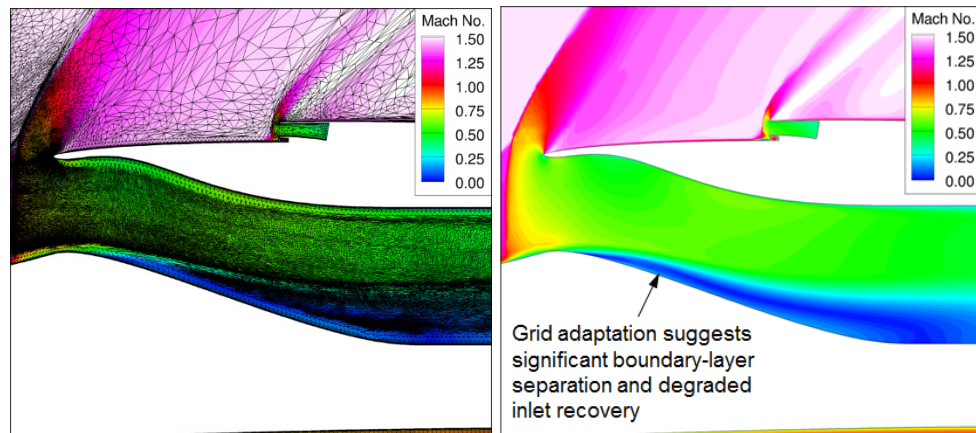


Figure 31.—Mach number contours for the 16 adaptation cycle pentahedral boundary-layer grid (case #8), $m_2/m_0 = 0.99$.

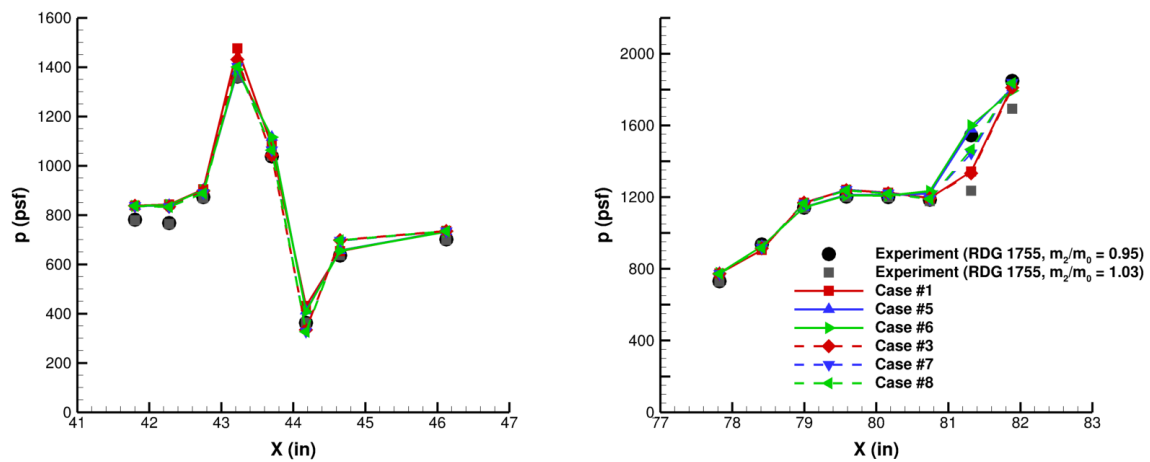


Figure 32.—Static pressure profiles along the camera fairing (left) and inlet bump (right) for $M_\infty = 1.46$, $\alpha = 2.0^\circ$.

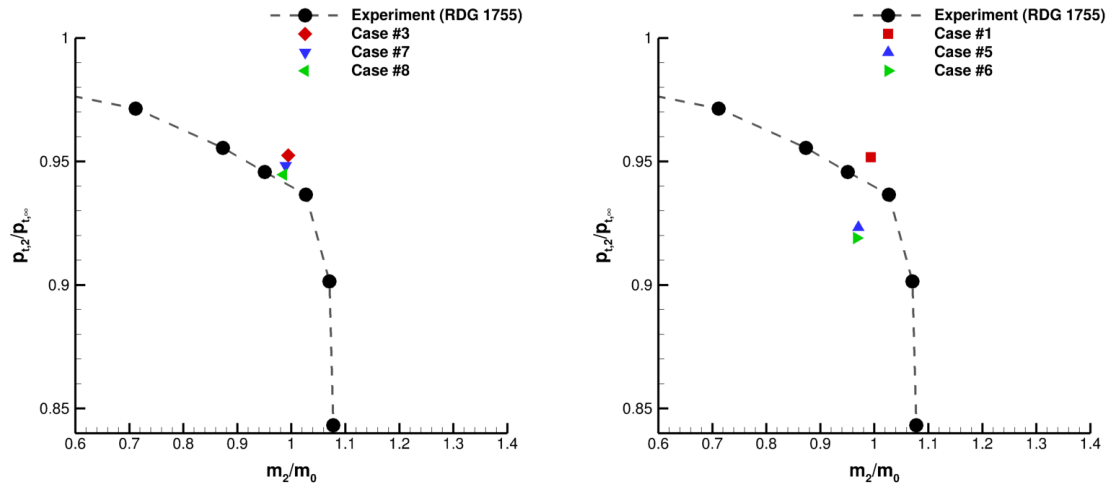


Figure 33.—The 40-probe total pressure recovery plots on the pentahedral boundary-layer grids (left) and on the tetrahedral boundary-layer grids (right) for $M_\infty = 1.46$, $\alpha = 2.0^\circ$.

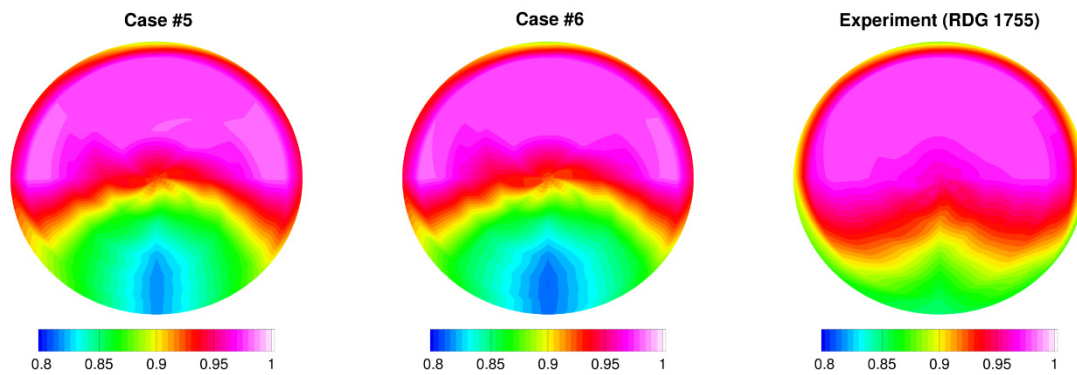


Figure 34.—The 40-probe total pressure recovery contours for the 8 adaptation cycle (left) and 16 adaptation cycle (middle) tetrahedral boundary-layer grids compared to the experiment (right) at $M_\infty = 1.46$, $\alpha = 2.0^\circ$.

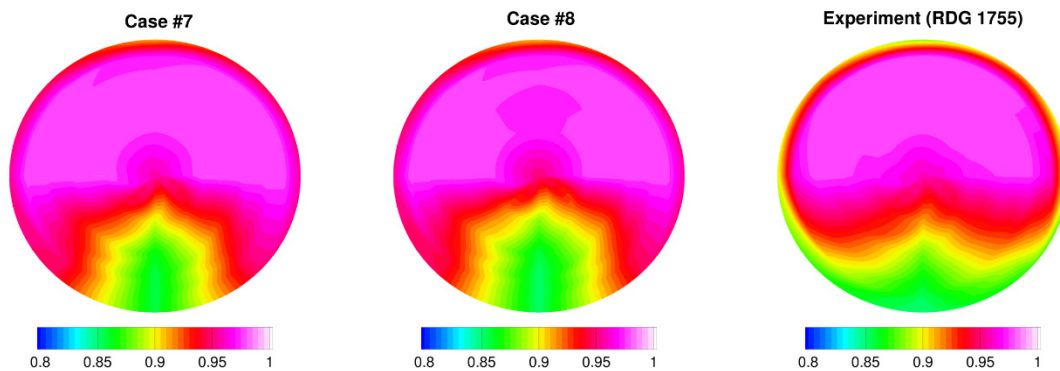


Figure 35.—The 40-probe total pressure recovery contours for the 8 adaptation cycle (left) and 16 adaptation cycle (middle) pentahedral boundary-layer grids compared to the experiment (right) at $M_\infty = 1.46$, $\alpha = 2.0^\circ$.

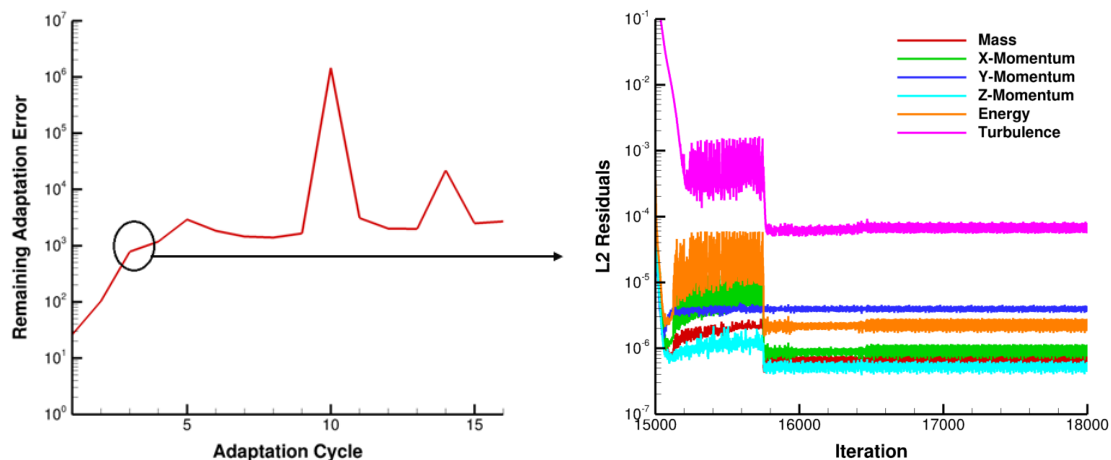


Figure 36.—Remaining adaptation error (left) and 3rd adaptation cycle flow residuals (right) for the pentahedral boundary-layer grid.

3.4 Manually Refined Grids

Figure 37 and Figure 38 show the Mach number contour plots along the aircraft centerline for the Reading 1755 conditions ($M_\infty = 1.46$, $\alpha = 2.0^\circ$) on the manually refined grids (cases #9 and #10). Just like on the adapted grids (cases #2, #4, #5, #6, #7, and #8), the CFD solutions predict a large separation region within the subsonic diffuser, regardless of the cell type within/around the boundary-layer regions. Figure 39 shows the static pressure profiles at the camera fairing and inlet bump for the reading 1755 conditions on the manually refined grids (cases #9 and #10). For comparison, the solutions on the unadapted (cases #1 and #3) and 16 adaptation cycle (cases #6 and #8) grids were included in the plots. The figure shows that the manually refined grids tend to agree with the unadapted and 16 adaptation cycle grids at the camera fairing with the exception of the fourth upstream location ($x = 43.2$ in.), where the manually refined grids predict a lower pressure than the 16 adaptation cycle grid. The figure also shows that the CFD solutions on the manually refined grids tend to agree with the other CFD solutions at the inlet bump with the exception of the second to last downstream location ($x = 81.3$ in.). At this location, the predicted pressure measurements on the manually refined grids match closely with the pressure measurements predicted on the unadapted grids.

Figure 40 shows the 40-probe average total pressure recovery for the manually refined grids along with the 40-probe average total pressure recoveries for the unadapted and 16 adaptation cycle grids. Interestingly, the figure shows that the average total pressure recovery on the manually refined pentahedral boundary-layer grid agrees with the unadapted pentahedral boundary-layer grid while the average total pressure recovery on the manually refined tetrahedral boundary-layer grid falls in between the unadapted and 16 adaptation cycle tetrahedral boundary-layer grids. One reason for this discrepancy between the two different cell-type grids could be that the phenomena that the total pressure recovery decreases asymptotically as the adaption cycle (and thus the grid size) is increased was more pronounced on the tetrahedral boundary-layer grids than the pentahedral boundary-layer grids. This would imply that one would expect a greater disagreement between the 40-probe average total pressure recoveries computed from the tetrahedral boundary-layer grids compared to those computed from the pentahedral boundary-layer grids. Figure 41 and Figure 42 show the 40-probe total pressure recovery contour plots for the manually refined grids compared to the unadapted and 16 adaptation cycle grids. It can be seen that the manually refined grids are predicting a region of lower total pressure recovery that is sized in between the equivalent regions predicted on the unadapted and 16 adaptation cycle grids. This makes sense as the number of nodes at the AIP on the manually refined grids was greater than the number of nodes on the unadapted grids but less than the number of nodes on the 16 adaptation cycle grids.

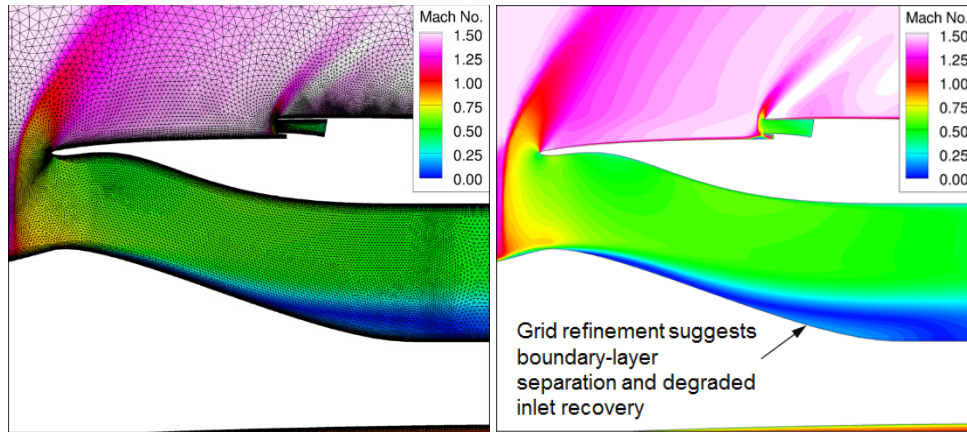


Figure 37.—Mach number contours for the manually refined tetrahedral boundary-layer grid (case #9), $m_2/m_0 = 0.99$.

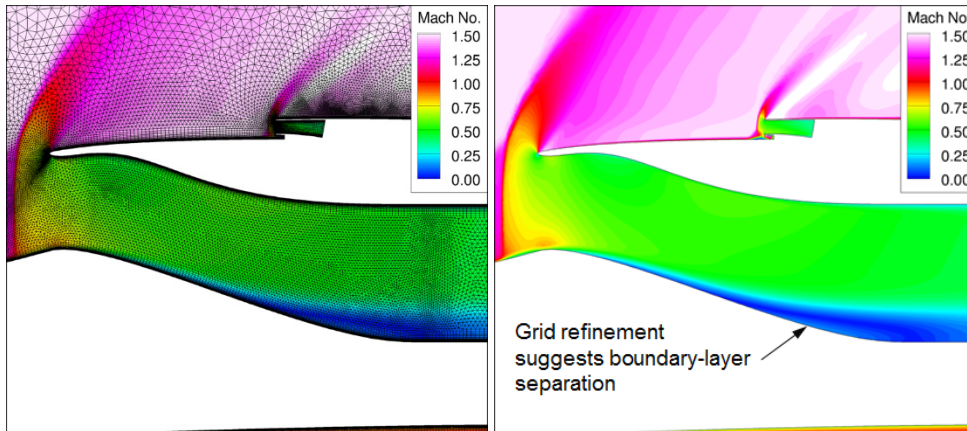


Figure 38.—Mach number contours for the manually refined pentahedral boundary-layer grid (case #10), $m_2/m_0 = 1.00$.

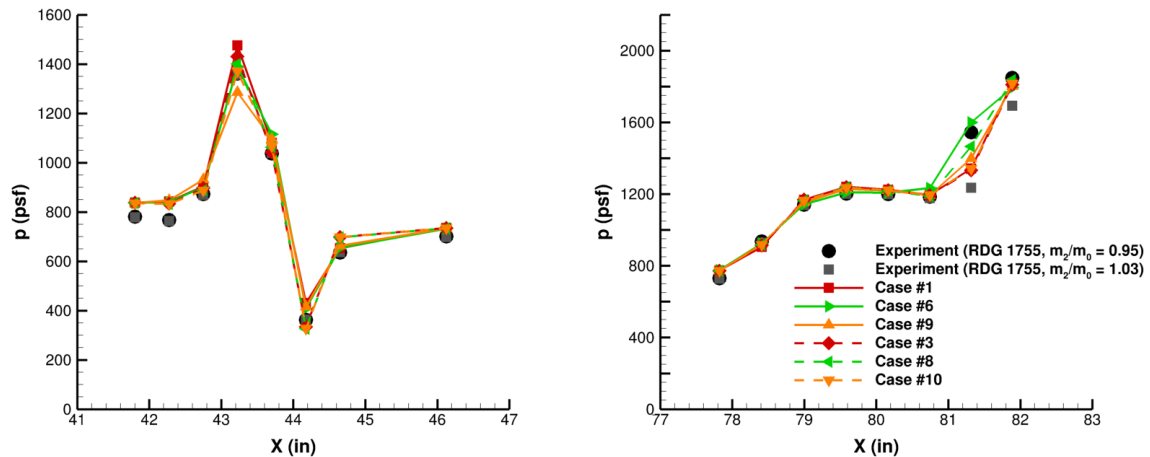


Figure 39.—Static pressure profiles along the camera fairing (left) and inlet bump (right) for $M_\infty = 1.46$, $\alpha = 2.0^\circ$.

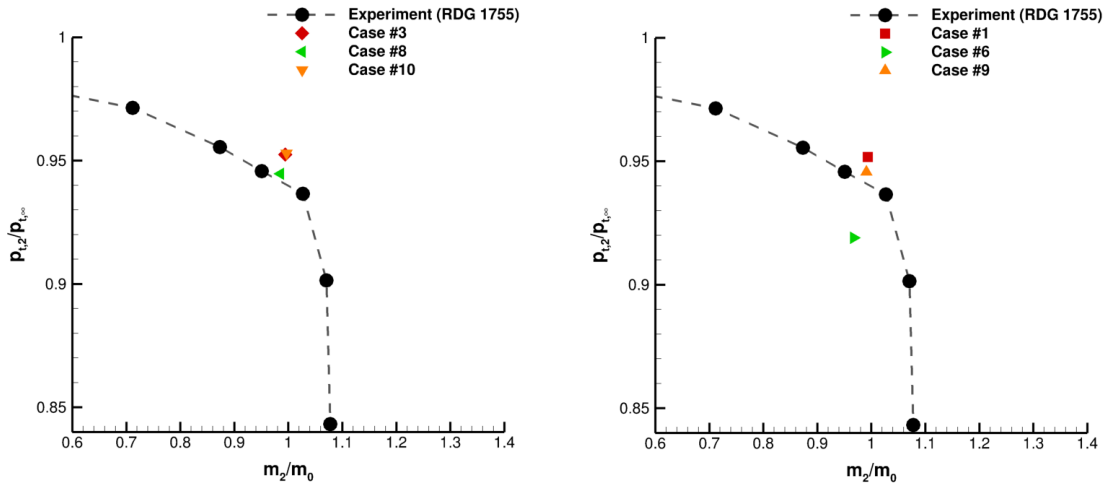


Figure 40.—The 40-probe total pressure recovery plots on the pentahedral boundary-layer grids (left) and on the tetrahedral boundary-layer grids (right) for $M_\infty = 1.46$, $\alpha = 2.0^\circ$.

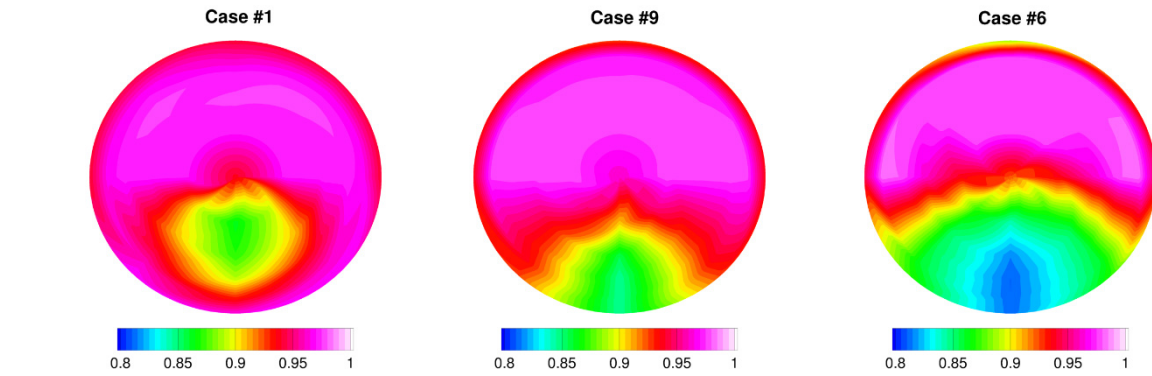


Figure 41.—The 40-probe total pressure recovery contours for the unadapted (left), manually refined (middle), and 16 adaptation cycle (right) tetrahedral boundary-layer grids at $M_\infty = 1.46$, $\alpha = 2.0^\circ$.

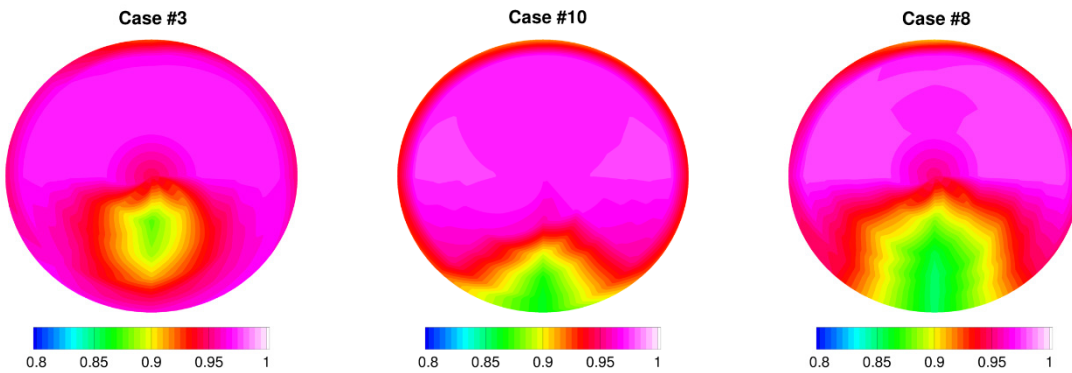


Figure 42.—The 40-probe total pressure recovery contours for the unadapted (left), manually refined (middle), and 16 adaptation cycle (right) pentahedral boundary-layer grids at $M_\infty = 1.46$, $\alpha = 2.0^\circ$.

3.5 Additional Simulations

Based on the results obtained on the adapted and manually refined grids, it was decided to run the simulations at the other two conditions using only the unadapted tetrahedral and pentahedral boundary-layer grids (cases #1 and #3). Figure 43 and Figure 44 show the aircraft centerline Mach number contours at the Reading 1771 conditions ($M_\infty = 1.35$, $\alpha = 3.0^\circ$) with an inlet mass flow rate ratio of 0.96. Both grids predict a small separation within the subsonic diffuser, a trend that is consistent with the sub-studies using these grids at the higher Mach number condition. Figure 45 and Figure 46 show the static pressure profiles at the camera fairing and inlet bump, respectively, for the CFD solutions on the unadapted tetrahedral boundary-layer grid and the experiment at various inlet mass flow rate ratios at the Reading 1771 condition. The figures show that the pressure profiles are insensitive to the inlet mass flow rate ratio at the camera fairing region and for the first five upstream pressure stations of the inlet bump region. However, the pressure measurements at the remaining three downstream pressure stations are shown to decrease as the mass flow rate ratio is increased. This is because the shockwave in front of the inlet moves downstream as the inlet mass flow rate ratio is increased. Note that the CFD solutions on the unadapted pentahedral boundary-layer grid were omitted from Figure 45 and Figure 46 as they displayed the same trend as the CFD solutions on the unadapted tetrahedral boundary-layer grid. To further compare the CFD solutions and the experimental data, the static pressure profiles at the camera fairing and inlet bump at an inlet mass flow rate ratio of 0.92 are shown in Figure 47. From an engineering perspective the pressure profiles at the camera fairing and at the inlet bump all agree with each other, which is also the case statistically. Most of the pressure profiles agree with each other statistically at the 95 percent confidence level, with the exception of comparing the CFD solutions to each other at $x = 79.0$ in. and downstream of $x = 79.6$ in. up until $x = 81.9$ in. In addition, the 40-probe average total pressure recovery values, shown in Figure 48, tend to agree statistically with the experimental data for both the unadapted tetrahedral and pentahedral boundary-layer grids at the 95 percent confidence level. This is further demonstrated in the 40-probe total pressure recovery contour plots, shown in Figure 49, although both CFD solutions tend to under predict the size of the lower total pressure recovery region.

Figure 50 and Figure 51 show the aircraft centerline Mach number contours at the Reading 2033 conditions ($M_\infty = 0.30$, $\alpha = 3.0^\circ$) at an inlet mass flow rate ratio of 1.81 for the unadapted tetrahedral boundary-layer grid and 1.82 for the unadapted pentahedral boundary-layer grid. Unlike the supersonic cases, the small separation region has moved from the bottom of the subsonic diffuser to the top. This is consistent between the two grids. Figure 52 and Figure 53 show the static pressure profiles at the camera fairing and inlet bump, respectively, for the CFD solutions on the unadapted tetrahedral boundary-layer grid and the experiment at various inlet mass flow rate ratios at the Reading 2033 condition. It can be seen that the pressure profiles at the camera fairing are insensitive to the inlet mass flow rate ratios. It can also be shown that the pressure profiles at the inlet bump are insensitive to the inlet mass flow rate for the three most (CFD) and two most (experiment) upstream pressure stations, at which point the pressure measurements decrease with increasing mass flow rate ratio. This trend is similar to what was seen at the Reading 1771 condition. However unlike the Reading 1771 condition which was at a supersonic freestream, the decrease in the pressure measurements as the mass flow rate ratio increases is not due to the movement of the external shockwave. To further compare the CFD solutions and the experimental data, the static pressure profiles at the camera fairing and the inlet bump at an inlet mass flow rate ratio of 1.86 are shown in Figure 54. While from an engineering perspective the static pressure profiles agree well with each other, this is further supported as they statistically agree with each other at the 95 percent confidence level. There are a few exceptions to this, specifically the CFD solutions compared to the experiment at the most downstream camera fairing pressure station and at the most downstream inlet bump pressure station. Figure 55 shows the respective 40-probe average total pressure recovery values, which show that the CFD solutions tend to agree well with each other and the experimental data. However, differences can be seen in the 40-probe total pressure recovery contour plots, shown in Figure 56. In particular, the CFD solutions tend to not fully capture the lower total pressure recovery region at the lower portion of AIP. Despite the statistical differences, the results of this sub-study suggest that FUN3D is able to better predict, from an engineering perspective, the flow field and inlet performance of a top-aft-mounted propulsion system as the freestream Mach number is decreased.

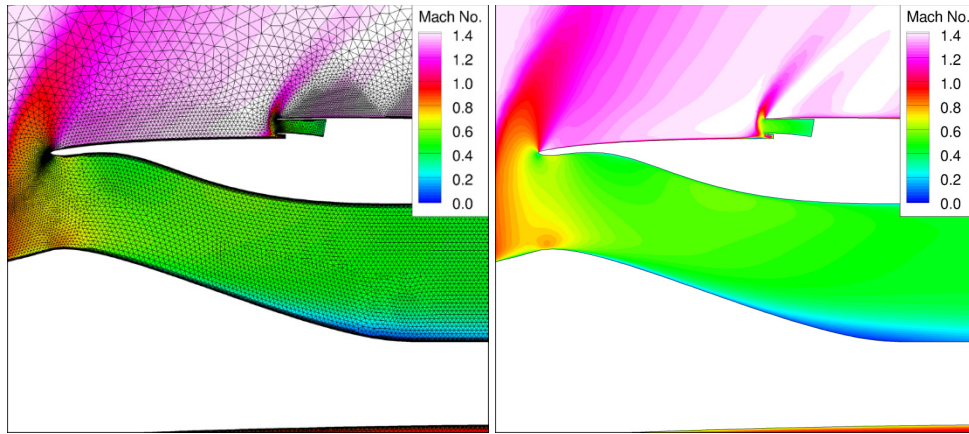


Figure 43.—Mach number contours for the unadapted tetrahedral boundary-layer grid (case #1) for $M_\infty = 1.35$, $\alpha = 3.0^\circ$, $m_2/m_0 = 0.96$.

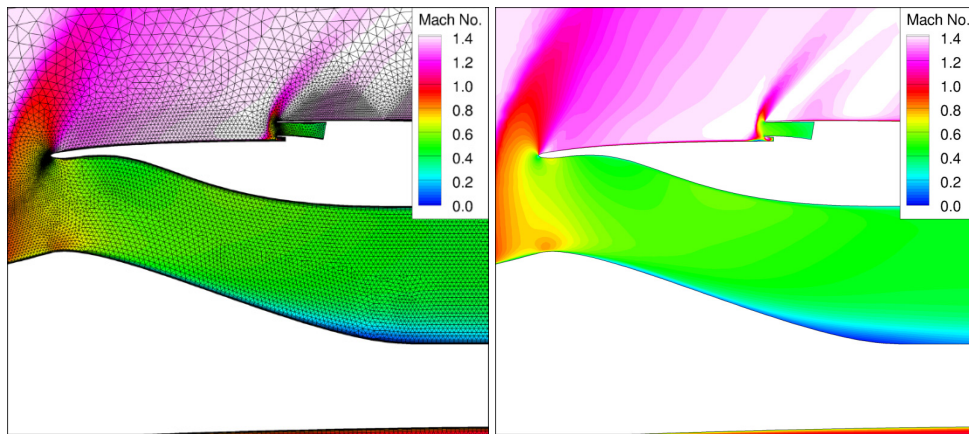


Figure 44.—Mach number contours for the unadapted pentahedral boundary-layer grid (case #3) for $M_\infty = 1.35$, $\alpha = 3.0^\circ$, $m_2/m_0 = 0.96$.

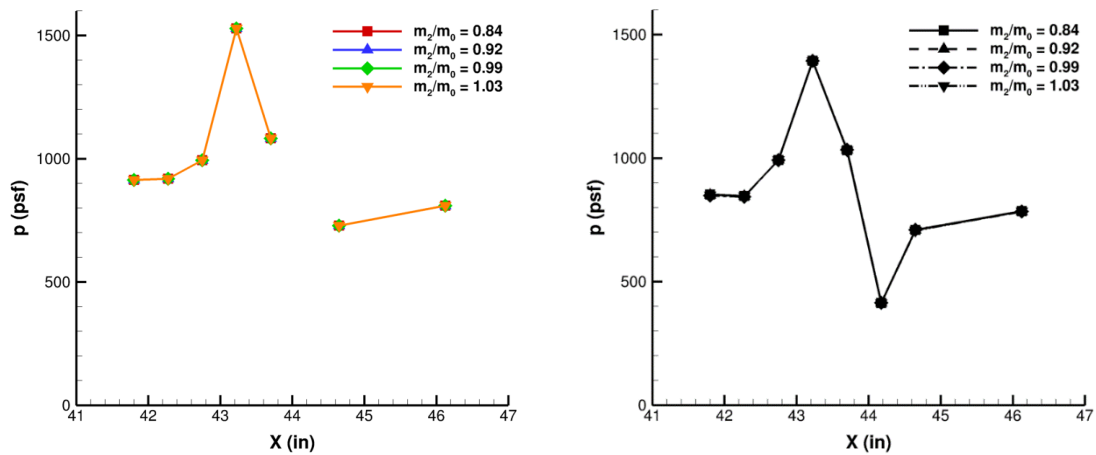


Figure 45.—Static pressure profiles along the camera fairing for the unadapted tetrahedral boundary-layer grid (case #1) (left) and the experiment (right) for $M_\infty = 1.35$, $\alpha = 3.0^\circ$.*

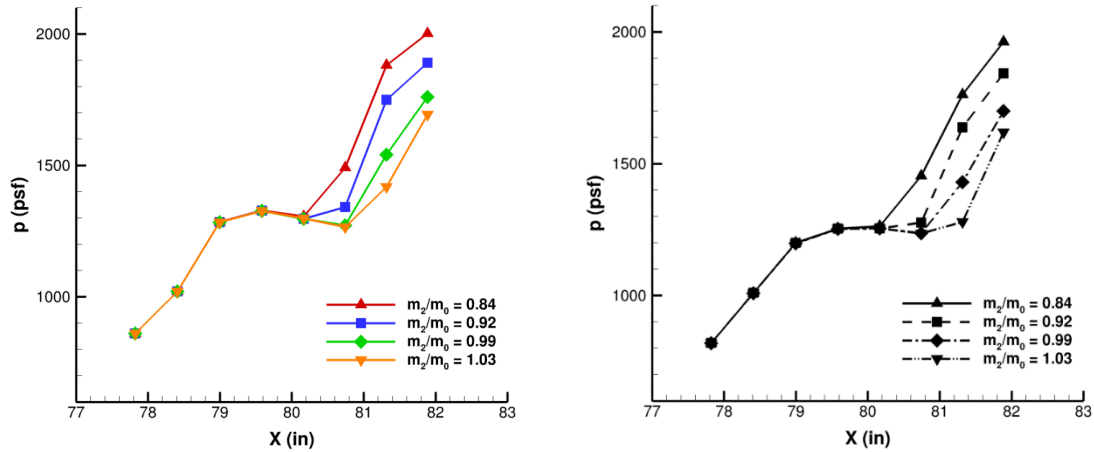


Figure 46.—Static pressure profiles along the inlet bump for the unadapted tetrahedral boundary-layer grid (case #1) (left) and the experiment (right) for $M_\infty = 1.35$, $\alpha = 3.0^\circ$.*

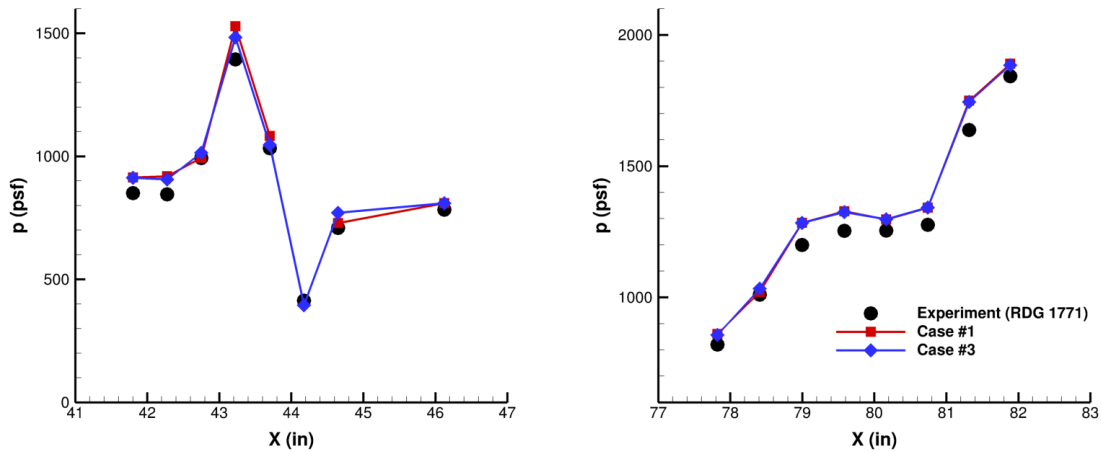


Figure 47.—Static pressure profiles along the camera fairing (left) and inlet bump (right) for $M_\infty = 1.35$, $\alpha = 3.0^\circ$, $m_2/m_0 = 0.92$.*

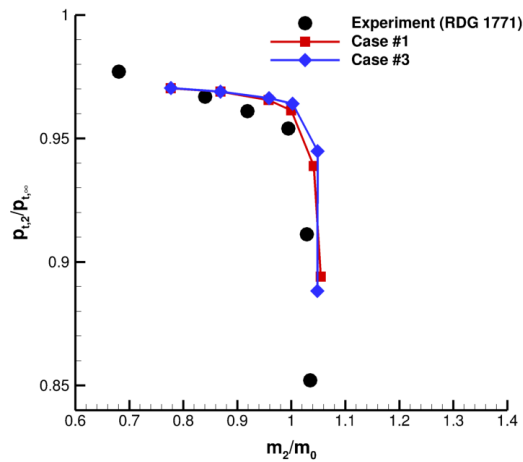


Figure 48.—The 40-probe total pressure recovery plot for $M_\infty = 1.35$, $\alpha = 3.0^\circ$.

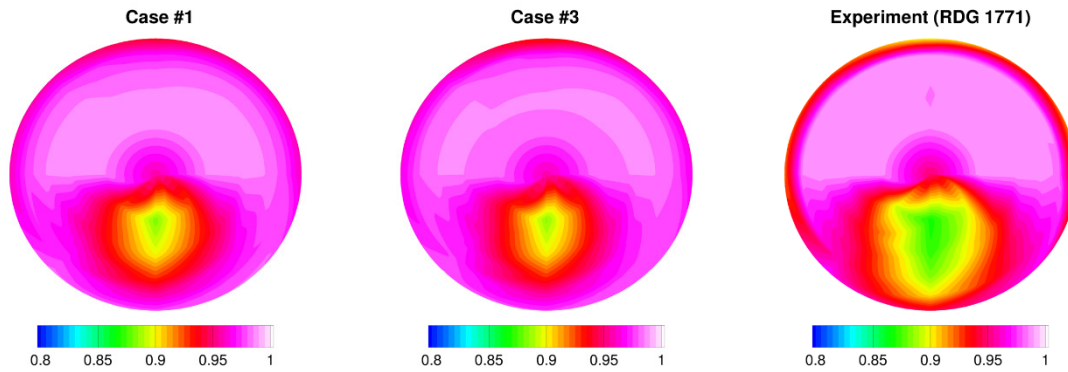


Figure 49.—The 40-probe total pressure recovery contours for the unadapted tetrahedral boundary-layer (left) and the unadapted pentahedral boundary-layer (middle) grids compared to the experiment (right) at $M_\infty = 1.35$, $\alpha = 3.0^\circ$.

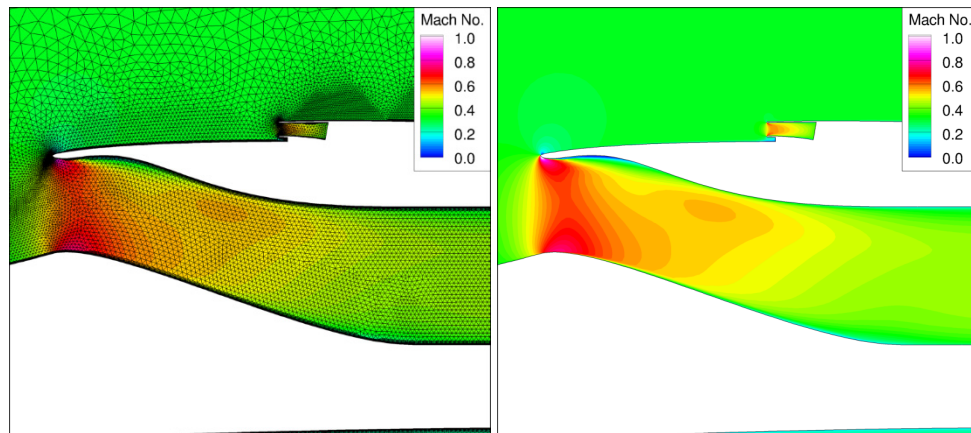


Figure 50.—Mach number contours for the unadapted tetrahedral boundary-layer grid (case #1) for $M_\infty = 0.30$, $\alpha = 3.0^\circ$, $m_2/m_0 = 1.81$.

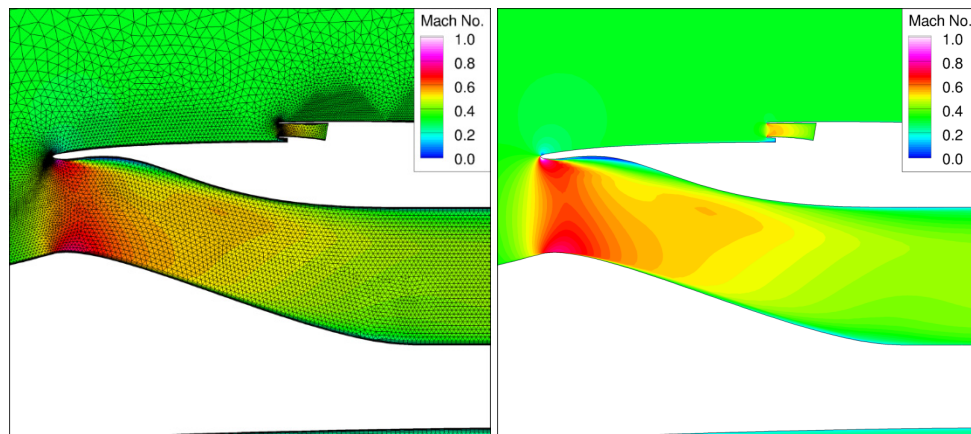


Figure 51.—Mach number contours for the unadapted pentahedral boundary-layer grid (case #3) for $M_\infty = 0.30$, $\alpha = 3.0^\circ$, $m_2/m_0 = 1.82$.

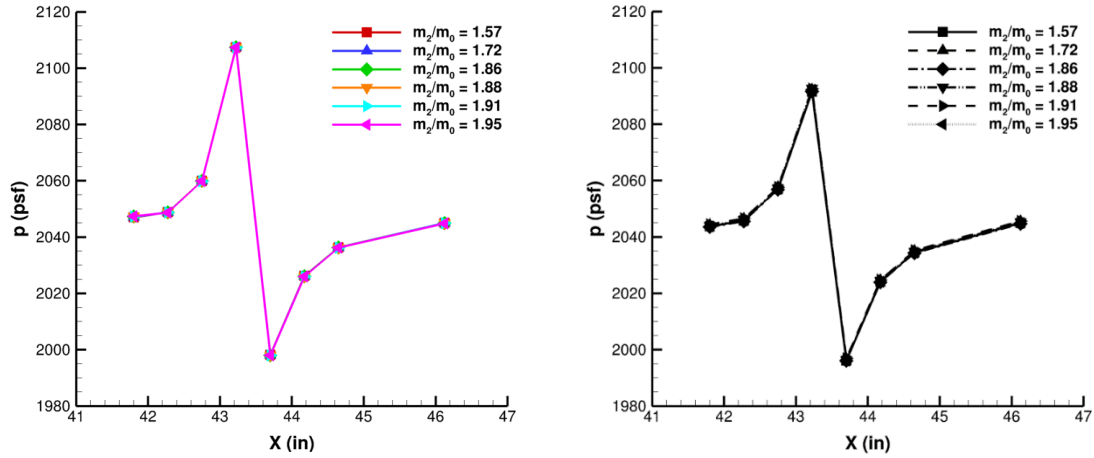


Figure 52.—Static pressure profiles along the camera fairing for the unadapted tetrahedral boundary-layer grid (case #1) (left) and the experiment (right) for $M_\infty = 0.30$, $\alpha = 3.0^\circ$.*

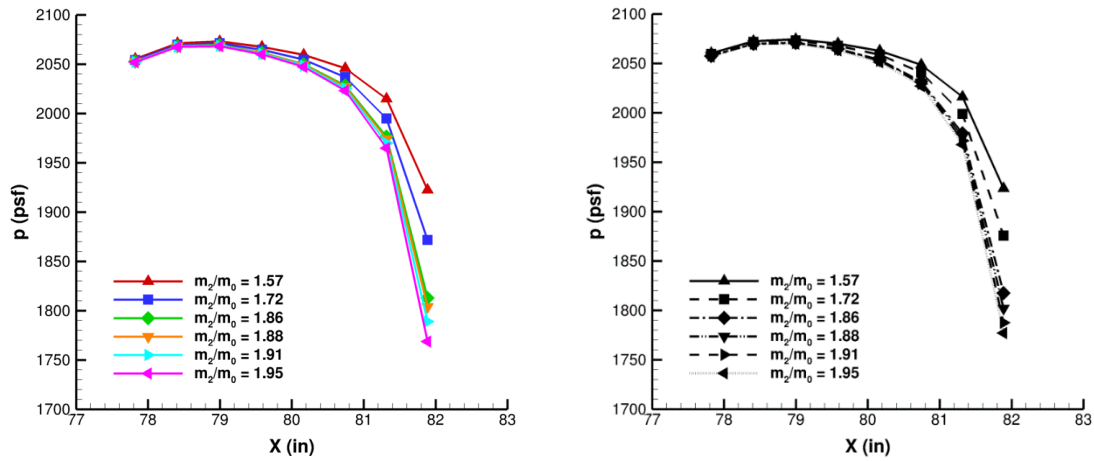


Figure 53.—Static pressure profiles along the inlet bump for the unadapted tetrahedral boundary-layer grid (case #1) (left) and the experiment (right) for $M_\infty = 0.30$, $\alpha = 3.0^\circ$.*

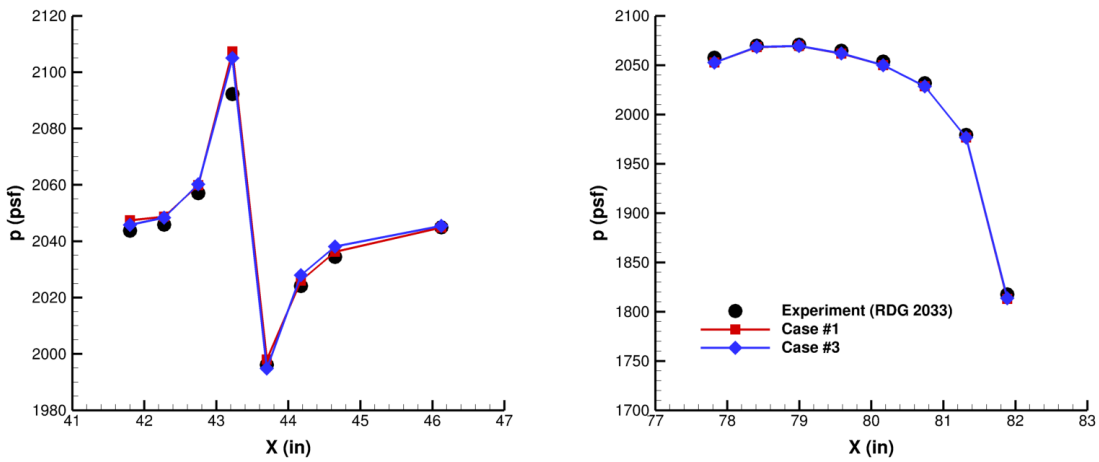


Figure 54.—Static pressure profiles along the camera fairing (left) and inlet bump (right) for $M_\infty = 0.30$, $\alpha = 3.0^\circ$, $m_2/m_0 = 1.86$.*

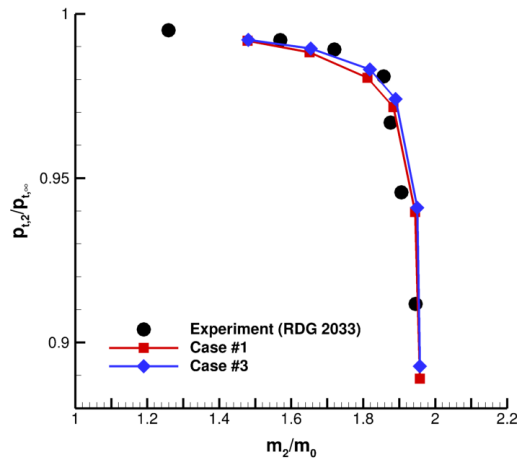


Figure 55.—The 40-probe total pressure recovery plot for $M_\infty = 0.30$, $\alpha = 3.0^\circ$.

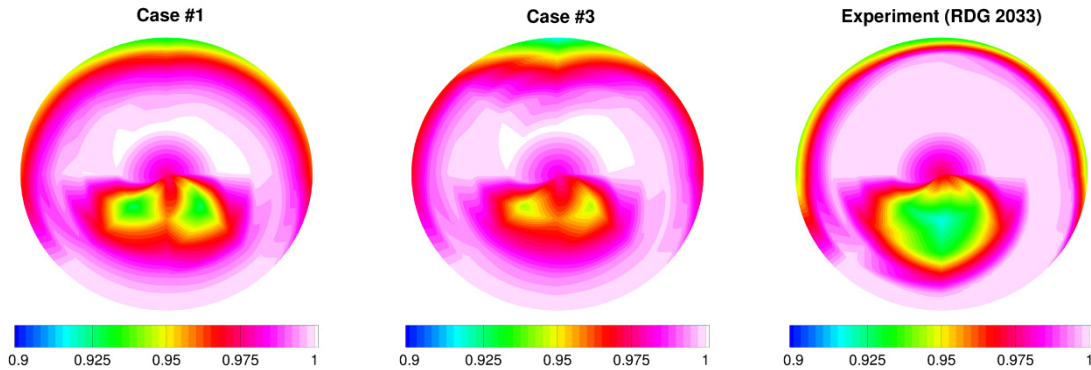


Figure 56.—The 40-probe total pressure recovery contours for the unadapted tetrahedral boundary-layer (left) and the unadapted pentahedral boundary-layer (middle) grids compared to the experiment (right) at $M_\infty = 0.30$, $\alpha = 3.0^\circ$.

4.0 Conclusions

To conclude, a grid adaptation study was performed on a QueSST aircraft preliminary design in order to determine internal “best practices” for computing inlet performance of top-aft-mounted inlets. It was shown that grids with pentahedral cells in/around the boundary-layer regions generally did slightly better at predicting inlet performance than grids with tetrahedral cells in that same region. It was also shown that both the engine axis-aligned linear pressure sensor and the pressure box objective led to adapted grids that poorly predicted inlet performance. In addition, it was shown that the 40-probe total pressure recovery decreases asymptotically as the number of adaptation cycles increases and agreement with the experimental data generally got worse with the number of adaptation cycles. Finally, it was shown that the CFD results on the unadapted grids had better agreement with the experimental data at the lower freestream Mach numbers compared to the freestream Mach number of 1.46. These trends suggest that predicting inlet performance with RANS CFD has a high uncertainty in the computed values for a high speed top-aft-mounted propulsion system without anchoring the CFD solutions to experimental data and performing a grid refinement study.

Appendix A.—CFD Inlet Mass Flow Rate Ratios

Tables A1 to A11 outline the inlet mass flow rate ratios that the CFD simulations were run at.

TABLE A1.—INLET MASS FLOW RATERATIOS FOR THE CELL
TYPE AND GRID ADAPTATION METRIC SUB-STUDY
[Tetrahedral boundary-layer grids, cases #1 and #2.]

Adaptation cycles	m_2/m_0
0	0.83
	0.88
	0.92
	0.96
	1.02
	1.05
	1.09
8	0.76
	0.81
	0.85
	0.89
	0.93
	0.96
	1.00
	1.07

TABLE A2.—INLET MASS FLOW RATE RATIOS FOR THE CELL
TYPE AND GRID ADAPTATION METRIC SUB-STUDY
[Pentahedral boundary-layer grids, cases #3 and #4.]

Adaptation cycles	m_2/m_0
0	0.75
	0.86
	0.95
	1.04
	1.08
	1.09
8	0.75
	0.80
	0.85
	0.89
	0.94
	0.99
	1.03
	1.07
	1.10

TABLE A3.—INLET MASS FLOW RATE RATIOS FOR THE CELL
TYPE AND GRID ADAPTATION METRIC SUB-STUDY
[Pentahedral boundary-layer smooth grid, case #3A.]

Adaptation cycles	m_2/m_0
0	0.86
	0.95
	1.04
	1.08
	1.09

TABLE A4.—INLET MASS FLOW RATE RATIOS FOR THE
NUMBER OF ADAPTATION CYCLES SUB-STUDY
[Tetrahedral boundary-layer grids, cases #1, #5, and #6.]

Adaptation cycles	m_2/m_0
0	0.99
^a 8	0.97
^a 16	0.97

^aReduced number of additional nodes/adaptation cycle.

TABLE A5.—INLET MASS FLOW RATE RATIOS FOR THE
NUMBER OF ADAPTATION CYCLES SUB-STUDY
[Pentahedral boundary-layer grids, cases #3, #7, and #8.]

Adaptation cycles	m_2/m_0
0	0.99
^a 8	0.99

^aReduced number of additional nodes/adaptation cycle.

TABLE A6.—INLET MASS FLOW RATE RATIOS FOR THE
MANUALLY REFINED GRID SUB-STUDY
[Tetrahedral boundary-layer grid, case #9.]

Adaptation cycles	m_2/m_0
0	0.99

TABLE A7.—INLET MASS FLOW RATE RATIOS FOR THE
MANUALLY REFINED GRID SUB-STUDY
[Pentahedral boundary-layer grid, case #10.]

Adaptation cycles	m_2/m_0
0	1.00

TABLE A8.—INLET MASS FLOW RATE RATIOS FOR THE
ADDITIONAL SIMULATIONS SUB-STUDY
[Reading 1771 conditions, tetrahedral boundary-layer grid, case #1.]

Adaptation cycles	m_2/m_0
0	0.78
	0.87
	0.96
	1.00
	1.04
	1.05

TABLE A9.—INLET MASS FLOW RATE RATIOS FOR THE
ADDITIONAL SIMULATIONS SUB-STUDY
[Reading 1771 conditions, pentahedral boundary-layer grid, case #3.]

Adaptation cycles	m_2/m_0
0	0.78
	0.87
	0.96
	1.00
	1.05
	1.05

TABLE A10.—INLET MASS FLOW RATE RATIOS FOR THE
ADDITIONAL SIMULATIONS SUB-STUDY
[Reading 2033 conditions, tetrahedral boundary-layer grid, case #1.]

Adaptation cycles	m_2/m_0
0	1.48
	1.65
	1.81
	1.88
	1.94
	1.96

TABLE A11.—INLET MASS FLOW RATE RATIOS FOR THE
ADDITIONAL SIMULATIONS SUB-STUDY
[Reading 2033 conditions, pentahedral boundary-layer grid, case #3.]

Adaptation cycles	m_2/m_0
0	1.48
	1.65
	1.82
	1.89
	1.95
	1.96

Appendix B.—CFD Curve Fits

This appendix contains the CFD curve fit equations and respective R-squared values. For the cases where the curve fit was determined to be a constant, the maximum minus minimum values are reported instead of the R-squared values. Curve fits with R-squared values less than 0.8 were omitted from this appendix as those curve fits were not used to perform the paired t-tests. For pressure station references, see Figure 7 in the Results section of the paper. For case number references, see Table 2.

For the cell type and grid adaptation metric sub-study (unadapted tetrahedral boundary-layer grid, case #1) at the camera fairing region:

$$p_{101} = 0.5601(m_2/m_0)^3 - 1.4542(m_2/m_0)^2 + 1.2537(m_2/m_0) + 836.86 \quad (\text{B1})$$

$$R_{p_{101}}^2 = 0.9387 \quad (\text{B1a})$$

$$p_{102} = 834.6363 \quad (\text{B2})$$

$$p_{102,max} - p_{102,min} = 0.0024 \quad (\text{B2a})$$

$$p_{103} = \begin{cases} 893.2497, (m_2/m_0) \leq 1.03 \\ 893.1452, (m_2/m_0) > 1.03 \end{cases} \quad (\text{B3})$$

$$p_{104} = \begin{cases} 0.1062(m_2/m_0)^2 + 0.1938(m_2/m_0) + 834.72, (m_2/m_0) \leq 1.03 \\ 893.1452, (m_2/m_0) > 1.03 \end{cases} \quad (\text{B4})$$

$$R_{p_{104}}^2 = 0.8713 \quad (\text{B4a})$$

$$p_{105} = \begin{cases} 1100.1956, (m_2/m_0) \leq 1.03 \\ 1100.2662, (m_2/m_0) > 1.03 \end{cases} \quad (\text{B5})$$

$$p_{106} = 479.7428 \quad (\text{B6})$$

$$p_{106,max} - p_{106,min} = 0.0360 \quad (\text{B6a})$$

$$p_{107} = 626.9048 \quad (\text{B7})$$

$$p_{107,max} - p_{107,min} = 0.1061 \quad (\text{B7a})$$

$$p_{108} = 728.7104 \quad (\text{B8})$$

$$p_{108,max} - p_{108,min} = 0.0055 \quad (\text{B8a})$$

For the cell type and grid adaptation metric sub-study (unadapted tetrahedral boundary-layer grid, case #1) at the inlet bump region:

$$p_{601} = 772.2966 \quad (B9)$$

$$p_{601,max} - p_{601,min} = 0.0083 \quad (B9a)$$

$$p_{602} = \begin{cases} 902.3095, (m_2/m_0) \leq 1.03 \\ 902.3285, (m_2/m_0) > 1.03 \end{cases} \quad (B10)$$

$$p_{603} = 2.4629(m_2/m_0)^2 - 4.7215(m_2/m_0) + 1177 \quad (B11)$$

$$R_{p_{603}}^2 = 0.8291 \quad (B11a)$$

$$p_{604} = 7.6848(m_2/m_0)^2 - 14.918(m_2/m_0) + 1247.5 \quad (B12)$$

$$R_{p_{604}}^2 = 0.8717 \quad (B12a)$$

$$p_{605} = -712.99 \left(\frac{m_2}{m_0}\right)^4 + 2856.5 \left(\frac{m_2}{m_0}\right)^3 - 4281.6 \left(\frac{m_2}{m_0}\right)^2 + 2844.8(m_2/m_0) + 515.34 \quad (B13)$$

$$R_{p_{605}}^2 = 0.9994 \quad (B13a)$$

$$p_{606} = -15737(m_2/m_0)^3 + 47384(m_2/m_0)^2 + 47441(m_2/m_0) + 16987 \quad (B14)$$

$$R_{p_{606}}^2 = 0.9914 \quad (B14a)$$

$$p_{607} = 79490(m_2/m_0)^3 - 228699(m_2/m_0)^2 + 215447(m_2/m_0) - 64888 \quad (B15)$$

$$R_{p_{607}}^2 = 0.9992 \quad (B15a)$$

$$p_{608} = -4816.5(m_2/m_0)^2 + 7280.5(m_2/m_0) - 665.28 \quad (B16)$$

$$R_{p_{608}}^2 = 0.9954 \quad (B16a)$$

For the cell type and grid adaptation metric sub-study (unadapted tetrahedral boundary-layer grid, case #1) circumferential and radial inlet distortion:

$$DPCP = 19.7(m_2/m_0)^3 - 54.31(m_2/m_0)^2 + 49.796(m_2/m_0) - 15.149 \quad (B17)$$

$$R_{DPCP}^2 = 0.9627 \quad (B17a)$$

$$DPRP = -2.774(m_2/m_0)^3 + 7.6645(m_2/m_0)^2 - 6.9641(m_2/m_0) + 2.1008 \quad (B18)$$

$$R_{DPRP}^2 = 0.9934 \quad (B18a)$$

For the cell type and grid adaptation metric sub-study (8 adaptation cycle tetrahedral boundary-layer grid, case #2) at the camera fairing region:

$$p_{101} = 836.2034 \quad (\text{B19})$$

$$p_{101,max} - p_{101,min} = 0.0011 \quad (\text{B19a})$$

$$p_{102} = 835.6486 \quad (\text{B20})$$

$$p_{102,max} - p_{102,min} = 0.0019 \quad (\text{B20a})$$

$$p_{103} = 904.3434 \quad (\text{B21})$$

$$p_{103,max} - p_{103,min} = 0.0025 \quad (\text{B21a})$$

$$p_{104} = 1385.5925 \quad (\text{B22})$$

$$p_{104,max} - p_{104,min} = 0.0133 \quad (\text{B22a})$$

$$p_{105} = 1167.8532 \quad (\text{B23})$$

$$p_{105,max} - p_{105,min} = 0.0053 \quad (\text{B23a})$$

$$p_{106} = 496.1785 \quad (\text{B24})$$

$$p_{106,max} - p_{106,min} = 0.0142 \quad (\text{B24a})$$

$$p_{107} = 625.5193 \quad (\text{B25})$$

$$p_{107,max} - p_{107,min} = 0.0532 \quad (\text{B25a})$$

$$p_{108} = 730.9800 \quad (\text{B26})$$

$$p_{108,max} - p_{108,min} = 0.0045 \quad (\text{B26a})$$

For the cell type and grid adaptation metric sub-study (8 adaptation cycle tetrahedral boundary-layer grid, case #2) at the inlet bump region:

$$p_{601} = 258.94 \left(\frac{m_2}{m_0} \right)^4 - 985.2525 \left(\frac{m_2}{m_0} \right)^3 + 1405.4 \left(\frac{m_2}{m_0} \right)^2 - 888.7 \left(\frac{m_2}{m_0} \right) + 985.45 \quad (\text{B27})$$

$$R_{p_{601}}^2 = 0.9945 \quad (\text{B27a})$$

$$p_{602} = 15964 \left(\frac{m_2}{m_0} \right)^4 - 61044 \left(\frac{m_2}{m_0} \right)^3 + 87350 \left(\frac{m_2}{m_0} \right)^2 - 55438 \left(\frac{m_2}{m_0} \right) + 14100 \quad (\text{B28})$$

$$R_{p_{602}}^2 = 0.9984 \quad (\text{B28a})$$

$$p_{603} = -12343(m_2/m_0)^3 + 36090(m_2/m_0)^2 - 35084(m_2/m_0) + 12475 \quad (\text{B29})$$

$$R_{p_{603}}^2 = 0.9977 \quad (\text{B29a})$$

$$p_{604} = -3217.7(m_2/m_0)^3 + 13357(m_2/m_0)^2 - 17054(m_2/m_0) + 8098.6 \quad (\text{B30})$$

$$R_{p_{604}}^2 = 0.9745 \quad (\text{B30a})$$

$$p_{605} = -344018\left(\frac{m_2}{m_0}\right)^4 + 1313124\left(\frac{m_2}{m_0}\right)^3 - 1865837\left(\frac{m_2}{m_0}\right)^2 + 1168305\left(\frac{m_2}{m_0}\right) - 270386 \quad (\text{B31})$$

$$R_{p_{605}}^2 = 0.9828 \quad (\text{B31a})$$

$$p_{606} = 814869\left(\frac{m_2}{m_0}\right)^4 - 2925006\left(\frac{m_2}{m_0}\right)^3 + 3908569\left(\frac{m_2}{m_0}\right)^2 - 2305400\left(\frac{m_2}{m_0}\right) + 508176 \quad (\text{B32})$$

$$R_{p_{606}}^2 = 0.9937 \quad (\text{B32a})$$

$$p_{607} = -57593(m_2/m_0)^3 + 147973(m_2/m_0)^2 - 125805(m_2/m_0) + 36963 \quad (\text{B33})$$

$$R_{p_{607}}^2 = 0.9776 \quad (\text{B33a})$$

$$p_{608} = -258611\left(\frac{m_2}{m_0}\right)^4 + 899602\left(\frac{m_2}{m_0}\right)^3 - 1165950\left(\frac{m_2}{m_0}\right)^2 + 667328\left(\frac{m_2}{m_0}\right) - 140662 \quad (\text{B34})$$

$$R_{p_{608}}^2 = 0.9853 \quad (\text{B34a})$$

For the cell type and grid adaptation metric sub-study (8 adaptation cycle tetrahedral boundary-layer grid, case #2) circumferential and radial inlet distortion:

$$DPCP = -2.061(m_2/m_0)^3 + 5.4121(m_2/m_0)^2 - 4.5135(m_2/m_0) + 1.2777 \quad (\text{B35})$$

$$R_{DPCP}^2 = 0.997 \quad (\text{B35a})$$

$$DPRP = 15.184\left(\frac{m_2}{m_0}\right)^4 - 58.042\left(\frac{m_2}{m_0}\right)^3 + 82.347\left(\frac{m_2}{m_0}\right)^2 - 51.325\left(\frac{m_2}{m_0}\right) + 11.869 \quad (\text{B36})$$

$$R_{DPRP}^2 = 0.9942 \quad (\text{B36a})$$

For the cell type and grid adaptation metric sub-study (unadapted pentahedral boundary-layer grid, case #3) at the camera fairing region:

$$p_{101} = 837.2716 \quad (\text{B37})$$

$$p_{101,max} - p_{101,min} = 0.0037 \quad (\text{B37a})$$

$$p_{102} = 834.0574 \quad (38)$$

$$p_{102,max} - p_{102,min} = 0.0068 \quad (B38a)$$

$$p_{103} = -1.7555(m_2/m_0)^3 - 0.14(m_2/m_0)^2 + 4.8534(m_2/m_0) + 894.62 \quad (B39)$$

$$R_{p_{103}}^2 = 0.9298 \quad (B39a)$$

$$p_{105} = 0.6078(m_2/m_0)^3 - 0.0725(m_2/m_0)^2 - 1.4889(m_2/m_0) + 1044.3 \quad (B40)$$

$$R_{p_{105}}^2 = 0.9107 \quad (B40a)$$

$$p_{106} = 4.1714(m_2/m_0)^3 - 9.5121(m_2/m_0)^2 + 6.7695(m_2/m_0) + 334.62 \quad (B41)$$

$$R_{p_{106}}^2 = 0.8806 \quad (B41a)$$

$$p_{107} = 698.2854 \quad (B42)$$

$$p_{107,max} - p_{107,min} = 0.0104 \quad (B42a)$$

$$p_{108} = -1.307(m_2/m_0)^3 + 2.5331(m_2/m_0)^2 - 1.311(m_2/m_0) + 735.05 \quad (B43)$$

$$R_{p_{108}}^2 = 0.8654 \quad (B43a)$$

For the cell type and grid adaptation metric sub-study (unadapted pentahedral boundary-layer grid, case #3) at the inlet bump region:

$$p_{601} = 771.7627 \quad (B44)$$

$$p_{601,max} - p_{601,min} = 0.0128 \quad (B44a)$$

$$p_{602} = 913.9840 \quad (B45)$$

$$p_{602,max} - p_{602,min} = 0.0046 \quad (B45a)$$

$$p_{603} = -0.6124(m_2/m_0)^3 + 3.6156(m_2/m_0)^2 - 5.2168(m_2/m_0) + 1171 \quad (B46)$$

$$R_{p_{603}}^2 = 0.9625 \quad (B46a)$$

$$p_{604} = -7.1038(m_2/m_0)^3 + 24.916(m_2/m_0)^2 - 28.116(m_2/m_0) + 1249.3 \quad (B47)$$

$$R_{p_{604}}^2 = 0.98 \quad (B47a)$$

$$p_{605} = -25.269(m_2/m_0)^3 + 78.109(m_2/m_0)^2 - 80.042(m_2/m_0) + 1248.6 \quad (B48)$$

$$R_{p_{605}}^2 = 0.995 \quad (B48a)$$

$$p_{606} = -30693(m_2/m_0)^3 + 90068(m_2/m_0)^2 - 87765(m_2/m_0) + 29588 \quad (B49)$$

$$R_{p_{606}}^2 = 0.9953 \quad (\text{B49a})$$

$$p_{607} = 40605(m_2/m_0)^3 - 114776(m_2/m_0)^2 + 104557(m_2/m_0) - 29040 \quad (\text{B50})$$

$$R_{p_{607}}^2 = 0.9861 \quad (\text{B50a})$$

$$p_{608} = -2443.7(m_2/m_0)^2 + 2780.8(m_2/m_0) + 1454.7 \quad (\text{B51})$$

$$R_{p_{608}}^2 = 0.9994 \quad (\text{B51a})$$

For the cell type and grid adaptation metric sub-study (unadapted pentahedral boundary-layer grid, case #3) circumferential and radial inlet distortion:

$$DPCP = 2.427(m_2/m_0)^3 - 6.402(m_2/m_0)^2 + 5.6683(m_2/m_0) - 1.6055 \quad (\text{B52})$$

$$R_{DPCP}^2 = 0.984 \quad (\text{B52a})$$

$$DPRP = -20.23 \left(\frac{m_2}{m_0}\right)^3 + 74.226 \left(\frac{m_2}{m_0}\right)^2 - 101.54 \left(\frac{m_2}{m_0}\right) + 61.465 \left(\frac{m_2}{m_0}\right) - 13.886 \quad (\text{B53})$$

$$R_{DPRP}^2 = 0.9978 \quad (\text{B53a})$$

For the cell type and grid adaptation metric sub-study (8 adaptation cycle pentahedral boundary-layer grid, case #4) at the camera fairing region:

$$p_{101} = 836.9731 \quad (\text{B54})$$

$$p_{101,max} - p_{101,min} = 0.0008 \quad (\text{B54a})$$

$$p_{102} = 832.8298 \quad (\text{B55})$$

$$p_{102,max} - p_{102,min} = 0.0010 \quad (\text{B55a})$$

$$p_{103} = 888.6717 \quad (\text{B56})$$

$$p_{103,max} - p_{103,min} = 0.0159 \quad (\text{B56a})$$

$$p_{104} = 1401.9209 \quad (\text{B57})$$

$$p_{104,max} - p_{104,min} = 0.0327 \quad (\text{B57a})$$

$$p_{105} = 1062.6874 \quad (\text{B58})$$

$$p_{105,max} - p_{105,min} = 0.0067 \quad (\text{B58a})$$

$$p_{106} = 327.7475 \quad (\text{B59})$$

$$p_{106,max} - p_{106,min} = 0.0089 \quad (\text{B59a})$$

$$p_{107} = 696.5526 \quad (\text{B60})$$

$$p_{107,max} - p_{107,min} = 0.0013 \quad (\text{B60a})$$

$$p_{108} = -0.067(m_2/m_0)^3 + 0.01645(m_2/m_0)^2 - 0.124(m_2/m_0) + 733.83 \quad (\text{B61})$$

$$R_{p_{108}}^2 = 0.8333 \quad (\text{B61a})$$

For the cell type and grid adaptation metric sub-study (8 adaptation cycle pentahedral boundary-layer grid, case #4) at the inlet bump region:

$$p_{601} = 772.9009 \quad (\text{B62})$$

$$p_{601,max} - p_{601,min} = 0.0003 \quad (\text{B62a})$$

$$p_{602} = -0.5307(m_2/m_0)^3 + 1.5336(m_2/m_0)^2 - 1.4736(m_2/m_0) + 917.75 \quad (\text{B63})$$

$$R_{p_{602}}^2 = 0.9929 \quad (\text{B63a})$$

$$p_{603} = -3.7891(m_2/m_0)^3 + 11.556(m_2/m_0)^2 - 11.746(m_2/m_0) + 1168.5 \quad (\text{B64})$$

$$R_{p_{603}}^2 = 0.9992 \quad (\text{B64a})$$

$$p_{604} = 1987.4 \left(\frac{m_2}{m_0}\right)^5 - 9537.5 \left(\frac{m_2}{m_0}\right)^4 + 18251 \left(\frac{m_2}{m_0}\right)^3 - 17405 \left(\frac{m_2}{m_0}\right)^2 + 8270.5(m_2/m_0) - 326.95 \quad (\text{B65})$$

$$R_{p_{604}}^2 = 0.9938 \quad (\text{B65a})$$

$$p_{605} = -59014 \left(\frac{m_2}{m_0}\right)^5 + 283444 \left(\frac{m_2}{m_0}\right)^4 - 542987 \left(\frac{m_2}{m_0}\right)^3 + 518554 \left(\frac{m_2}{m_0}\right)^2 - 246855(m_2/m_0) + 48079 \quad (\text{B66})$$

$$R_{p_{605}}^2 = 0.9973 \quad (\text{B66a})$$

$$p_{606} = -25424(m_2/m_0)^3 + 78184(m_2/m_0)^2 - 79967(m_2/m_0) + 28391 \quad (\text{B67})$$

$$R_{p_{606}}^2 = 0.9919 \quad (\text{B67a})$$

$$p_{607} = 316304 \left(\frac{m_2}{m_0}\right)^4 - 1E6 \left(\frac{m_2}{m_0}\right)^3 + 2E6 \left(\frac{m_2}{m_0}\right)^2 - 891320 \left(\frac{m_2}{m_0}\right) + 197350 \quad (\text{B68})$$

$$R_{p_{607}}^2 = 0.9972 \quad (\text{B68a})$$

$$p_{608} = 8552.8(m_2/m_0)^3 - 27951(m_2/m_0)^2 + 27917(m_2/m_0) - 6708.9 \quad (\text{B69})$$

$$R_{p_{608}}^2 = 0.9987 \quad (\text{B69a})$$

For the cell type and grid adaptation metric sub-study (8 adaptation cycle pentahedral boundary-layer grid, case #4) circumferential and radial inlet distortion:

$$DPCP = -0.1281(m_2/m_0)^2 + 0.396(m_2/m_0) - 0.1573 \quad (B70)$$

$$R_{DPCP}^2 = 0.9937 \quad (B70a)$$

$$DPRP = 0.225(m_2/m_0)^2 - 0.3492(m_2/m_0) + 0.1461 \quad (B71)$$

$$R_{DPRP}^2 = 0.9959 \quad (B71a)$$

For the cell type and grid adaptation metric sub-study (unadapted pentahedral boundary-layer smooth grid, case #3A) at the camera fairing region:

$$p_{101} = 836.0603 \quad (B72)$$

$$p_{101,max} - p_{101,min} = 0.0005 \quad (B72a)$$

$$p_{102} = 832.9020 \quad (B73)$$

$$p_{102,max} - p_{102,min} = 0.0007 \quad (B73a)$$

$$p_{103} = 899.0945 \quad (B74)$$

$$p_{103,max} - p_{103,min} = 0.0027 \quad (B74a)$$

$$p_{104} = 1347.9143 \quad (B75)$$

$$p_{104,max} - p_{104,min} = 0.0056 \quad (B75a)$$

$$p_{105} = 1065.4308 \quad (B76)$$

$$p_{105,max} - p_{105,min} = 0.0020 \quad (B76a)$$

$$p_{107} = 698.2223 \quad (B77)$$

$$p_{107,max} - p_{107,min} = 0.0012 \quad (B77a)$$

$$p_{108} = 735.0952 \quad (B78)$$

$$p_{108,max} - p_{108,min} = 0.0007 \quad (B78a)$$

For the cell type and grid adaptation metric sub-study (unadapted pentahedral boundary-layer smooth grid, case #3A) at the inlet bump region:

$$p_{601} = 771.5815 \quad (B79)$$

$$p_{601,max} - p_{601,min} = 0.0011 \quad (B79a)$$

$$p_{602} = 916.4587 \quad (B80)$$

$$p_{602,max} - p_{602,min} = 0.0014 \quad (B81a)$$

$$p_{603} = 0.0611(m_2/m_0)^2 - 0.1341(m_2/m_0) + 1165.7 \quad (B82)$$

$$R_{p_{603}}^2 = 0.8997 \quad (B82a)$$

$$p_{604} = 0.3325(m_2/m_0)^2 - 0.6886(m_2/m_0) + 1233.7 \quad (B83)$$

$$R_{p_{604}}^2 = 0.9779 \quad (B83a)$$

$$p_{605} = -4.0325(m_2/m_0)^3 + 12.546(m_2/m_0)^2 - 13.018(m_2/m_0) + 1225.2 \quad (B84)$$

$$R_{p_{605}}^2 = 0.9991 \quad (B85a)$$

$$p_{606} = -1923.7(m_2/m_0)^3 + 5909.9(m_2/m_0)^2 - 6043.2(m_2/m_0) + 3250.7 \quad (B86)$$

$$R_{p_{606}}^2 = 0.9998 \quad (B86a)$$

$$p_{607} = 194573(m_2/m_0)^3 - 565950(m_2/m_0)^2 + 543483(m_2/m_0) - 170780 \quad (B87)$$

$$R_{p_{607}}^2 = 0.9992 \quad (B87a)$$

$$p_{608} = -3253.9(m_2/m_0)^2 + 4392.6(m_2/m_0) + 662.17 \quad (B88)$$

$$R_{p_{608}}^2 = 0.9993 \quad (B88a)$$

For the cell type and grid adaptation metric sub-study (unadapted pentahedral boundary-layer smooth grid, case #3A) circumferential and radial inlet distortion:

$$DPCP = 32.573(m_2/m_0)^3 - 93.237(m_2/m_0)^2 + 88.768(m_2/m_0) - 28.069 \quad (B89)$$

$$R_{DPCP}^2 = 0.8301 \quad (B89a)$$

$$DPRP = -4.9406(m_2/m_0)^3 + 14.342(m_2/m_0)^2 - 13.715(m_2/m_0) + 4.3547 \quad (B90)$$

$$R_{DPRP}^2 = 0.9635 \quad (B90a)$$

For the additional simulations sub-study (Reading 1771 conditions, unadapted tetrahedral boundary-layer grid, case #1) at the camera fairing region:

$$p_{101} = 913.4770 \quad (B91)$$

$$p_{101,max} - p_{101,min} = 0.0065 \quad (B91a)$$

$$p_{102} = 918.5313 \quad (B92)$$

$$p_{102,max} - p_{102,min} = 0.0041 \quad (B92a)$$

$$p_{103} = 993.3643 \quad (B93)$$

$$p_{103,max} - p_{103,min} = 0.0050 \quad (B93a)$$

$$p_{104} = 1528.8433 \quad (B94)$$

$$p_{104,max} - p_{104,min} = 0.0133 \quad (B94a)$$

$$p_{105} = 1082.5763 \quad (B95)$$

$$p_{105,max} - p_{105,min} = 0.0387 \quad (B95a)$$

$$p_{106} = 506.0323 \quad (B96)$$

$$p_{106,max} - p_{106,min} = 0.0462 \quad (B96a)$$

$$p_{107} = 728.6263 \quad (B97)$$

$$p_{107,max} - p_{107,min} = 0.0090 \quad (B97a)$$

$$p_{108} = 809.1670 \quad (B98)$$

$$p_{108,max} - p_{108,min} = 0.0020 \quad (B98a)$$

For the additional simulations sub-study (Reading 1771 conditions, unadapted tetrahedral boundary-layer grid, case #1) at the inlet bump region:

$$p_{601} = 0.559(m_2/m_0)^2 - 1.1337(m_2/m_0) + 860.79 \quad (B99)$$

$$R_{p_{601}}^2 = 0.9719 \quad (B99a)$$

$$p_{602} = 7.5182(m_2/m_0)^2 - 15.177(m_2/m_0) + 1028.2 \quad (B100)$$

$$R_{p_{602}}^2 = 0.9916 \quad (B100a)$$

$$p_{603} = 29.333(m_2/m_0)^2 - 59.247(m_2/m_0) + 1313.4 \quad (B101)$$

$$R_{p_{603}}^2 = 0.9926 \quad (B101a)$$

$$p_{604} = 47.361 \left(\frac{m_2}{m_0} \right)^2 - 95.631 \left(\frac{m_2}{m_0} \right) + 1375.4 \quad (B102)$$

$$R_{p_{604}}^2 = 0.9915 \quad (B102a)$$

$$p_{605} = -5722.4(m_2/m_0)^3 + 16697(m_2/m_0)^2 - 16205(m_2/m_0) + 6528.5 \quad (B103)$$

$$R_{p_{605}}^2 = 0.9987 \quad (B103a)$$

$$p_{606} = 6498.2(m_2/m_0)^2 - 1335.2(m_2/m_0) + 8123.8 \quad (B104)$$

$$R_{p_{606}}^2 = 0.9993 \quad (\text{B104a})$$

$$p_{607} = -7080.5(m_2/m_0)^2 + 10776(m_2/m_0) - 2174 \quad (\text{B105})$$

$$R_{p_{607}}^2 = 0.9964 \quad (\text{B105a})$$

$$p_{608} = -1974.5(m_2/m_0)^2 + 2052.1(m_2/m_0) + 1672 \quad (\text{B106})$$

$$R_{p_{608}}^2 = 0.9998 \quad (\text{B106a})$$

For the additional simulations sub-study (Reading 1771 conditions, unadapted pentahedral boundary-layer grid, case #3) at the camera fairing region:

$$p_{101} = 0.0233(m_2/m_0)^2 - 0.0323(m_2/m_0) + 912.41 \quad (\text{B107})$$

$$R_{p_{101}}^2 = 0.9912 \quad (\text{B107a})$$

$$p_{101} = 0.0398(m_2/m_0)^2 - 0.0626(m_2/m_0) + 906.49 \quad (\text{B108})$$

$$R_{p_{102}}^2 = 0.9856 \quad (\text{B108a})$$

$$p_{103} = -4.2094(m_2/m_0)^3 + 11.398(m_2/m_0)^2 - 10.177(m_2/m_0) + 1017.1 \quad (\text{B109})$$

$$R_{p_{103}}^2 = 0.8879 \quad (\text{B109a})$$

$$p_{104} = 6.4489(m_2/m_0)^3 - 17.177(m_2/m_0)^2 + 15.085(m_2/m_0) + 1479.3 \quad (\text{B110})$$

$$R_{p_{104}}^2 = 0.8613 \quad (\text{B110a})$$

$$p_{105} = 0.9737(m_2/m_0)^3 - 2.3054(m_2/m_0)^2 + 1.7606(m_2/m_0) + 1045.6 \quad (\text{B111})$$

$$R_{p_{105}}^2 = 0.9565 \quad (\text{B111a})$$

$$p_{106} = 395.0904 \quad (\text{B112})$$

$$p_{106,max} - p_{106,min} = 0.0096 \quad (\text{B112a})$$

$$p_{107} = -1.0958(m_2/m_0)^3 + 2.9705(m_2/m_0)^2 - 2.6606(m_2/m_0) + 771.46 \quad (\text{B113})$$

$$R_{p_{107}}^2 = 0.8495 \quad (\text{B113a})$$

$$p_{108} = 809.7467 \quad (\text{B114})$$

$$p_{108,max} - p_{108,min} = 0.0008 \quad (\text{B114a})$$

For the additional simulations sub-study (Reading 1771 conditions, unadapted pentahedral boundary-layer grid, case #3) at the inlet bump region:

$$p_{601} = 856.3335 \quad (\text{B115})$$

$$p_{601,max} - p_{601,min} = 0.0042 \quad (\text{B115a})$$

$$p_{602} = -15.435(m_2/m_0)^3 + 45.338(m_2/m_0)^2 - 44.434(m_2/m_0) + 1047.9 \quad (\text{B116})$$

$$R_{p_{602}}^2 = 0.9992 \quad (\text{B116a})$$

$$p_{603} = -65.145(m_2/m_0)^3 + 194.92(m_2/m_0)^2 - 194.64(m_2/m_0) + 1348.9 \quad (\text{B117})$$

$$R_{p_{603}}^2 = 0.9998 \quad (\text{B117a})$$

$$p_{604} = -124.11(m_2/m_0)^3 + 372.8(m_2/m_0)^2 - 373.64(m_2/m_0) + 1449.5 \quad (\text{B118})$$

$$R_{p_{604}}^2 = 0.9999 \quad (\text{B118a})$$

$$p_{605} = -3252.9(m_2/m_0)^3 + 9453.1(m_2/m_0)^2 - 9136.1(m_2/m_0) + 4234.6 \quad (\text{B119})$$

$$R_{p_{605}}^2 = 0.9986 \quad (\text{B119a})$$

$$p_{606} = 6395.9(m_2/m_0)^2 - 13171(m_2/m_0) + 8044.5 \quad (\text{B120})$$

$$R_{p_{606}}^2 = 0.9922 \quad (\text{B120a})$$

$$p_{607} = -35634(m_2/m_0)^3 + 90492(m_2/m_0)^2 - 77711(m_2/m_0) + 24392 \quad (\text{B121})$$

$$R_{p_{607}}^2 = 0.9997 \quad (\text{B121a})$$

$$p_{608} = -1860.1(m_2/m_0)^2 + 1823.8(m_2/m_0) + 1779.1 \quad (\text{B122})$$

$$R_{p_{608}}^2 = 0.9999 \quad (\text{B122a})$$

For the additional simulations sub-study (Reading 2033 conditions, unadapted tetrahedral boundary-layer grid, case #1) at the camera fairing region:

$$p_{101} = -0.4772(m_2/m_0)^2 + 1.381(m_2/m_0) + 2044.9 \quad (\text{B123})$$

$$R_{p_{101}}^2 = 0.8863 \quad (\text{B123a})$$

$$p_{102} = -2.025(m_2/m_0)^3 + 10.215(m_2/m_0)^2 - 17.333(m_2/m_0) + 2058.7 \quad (\text{B124})$$

$$R_{p_{102}}^2 = 0.9798 \quad (\text{B124a})$$

$$p_{103} = -4.3903(m_2/m_0)^3 + 22.134(m_2/m_0)^2 - 37.201(m_2/m_0) + 2080.8 \quad (\text{B125})$$

$$R_{p_{103}}^2 = 0.8987 \quad (\text{B125a})$$

$$p_{104} = -0.2105(m_2/m_0)^2 + 0.5449(m_2/m_0) + 2107.1 \quad (\text{B126})$$

$$R_{p_{104}}^2 = 0.998 \quad (\text{B126a})$$

$$p_{105} = 7.2561(m_2/m_0)^3 - 36.504(m_2/m_0)^2 + 60.424(m_2/m_0) + 1965.2 \quad (\text{B127})$$

$$R_{p_{105}}^2 = 0.8676 \quad (\text{B127a})$$

$$p_{106} = -0.522(m_2/m_0)^2 + 1.474(m_2/m_0) + 2024.5 \quad (\text{B128})$$

$$R_{p_{106}}^2 = 0.9063 \quad (\text{B128a})$$

$$p_{107} = -1.7652(m_2/m_0)^3 + 8.88(m_2/m_0)^2 - 15.102(m_2/m_0) + 2045 \quad (\text{B129})$$

$$R_{p_{107}}^2 = 0.98 \quad (\text{B129a})$$

$$p_{108} = -3.6472(m_2/m_0)^3 - 18.365(m_2/m_0)^2 - 30.927(m_2/m_0) + 2062.4 \quad (\text{B130})$$

$$R_{p_{108}}^2 = 0.9399 \quad (\text{B130a})$$

For the additional simulations sub-study (Reading 2033 conditions, unadapted tetrahedral boundary-layer grid, case #1) at the inlet bump region:

$$p_{601} = -8.992(m_2/m_0) + 2069.4 \quad (\text{B131})$$

$$R_{p_{601}}^2 = 0.9999 \quad (\text{B131a})$$

$$p_{602} = -9.7624(m_2/m_0) + 2086.4 \quad (\text{B132})$$

$$R_{p_{602}}^2 = 0.9996 \quad (\text{B132a})$$

$$p_{603} = -13.142(m_2/m_0) + 2093.7 \quad (\text{B133})$$

$$R_{p_{603}}^2 = 0.9997 \quad (\text{B133a})$$

$$p_{604} = -19.961(m_2/m_0) + 2098.8 \quad (\text{B134})$$

$$R_{p_{604}}^2 = 0.9996 \quad (\text{B134a})$$

$$p_{605} = -32.943(m_2/m_0) + 2111.2 \quad (\text{B135})$$

$$R_{p_{605}}^2 = 0.9993 \quad (\text{B135a})$$

$$p_{606} = -60.703(m_2/m_0) + 2141.1 \quad (\text{B136})$$

$$R_{p_{606}}^2 = 0.9987 \quad (\text{B136a})$$

$$p_{607} = -133.22(m_2/m_0) + 2223.9 \quad (\text{B137})$$

$$R_{p_{607}}^2 = 0.9967 \quad (\text{B137a})$$

$$p_{608} = -311.96(m_2/m_0)^2 + 687.91(m_2/m_0) + 1611.2 \quad (\text{B138})$$

$$R_{p_{608}}^2 = 0.9999 \quad (\text{B139a})$$

For the additional simulations sub-study (Reading 2033 conditions, unadapted pentahedral boundary-layer grid, case #3) at the camera fairing region:

$$p_{101} = -1.4129(m_2/m_0)^3 + 7.1302(m_2/m_0)^2 - 12.183(m_2/m_0) + 2052.9 \quad (\text{B140})$$

$$R_{p_{101}}^2 = 0.9829 \quad (\text{B140a})$$

$$p_{102} = -1.5645(m_2/m_0)^3 + 7.8982(m_2/m_0)^2 - 13.47(m_2/m_0) + 2056.2 \quad (\text{B141})$$

$$R_{p_{102}}^2 = 0.9809 \quad (\text{B142a})$$

$$p_{103} = -0.254(m_2/m_0) + 2060.7 \quad (\text{B143})$$

$$R_{p_{103}}^2 = 0.9995 \quad (\text{B143a})$$

$$p_{104} = -0.1758(m_2/m_0) + 2105.4 \quad (\text{B144})$$

$$R_{p_{104}}^2 = 0.999 \quad (\text{B144a})$$

$$p_{105} = -0.3804(m_2/m_0) + 1995.6 \quad (\text{B145})$$

$$R_{p_{105}}^2 = 0.9993 \quad (\text{B145a})$$

$$p_{106} = -5.5683(m_2/m_0)^3 + 28.115(m_2/m_0)^2 - 47.325(m_2/m_0) + 2054.6 \quad (\text{B146})$$

$$R_{p_{106}}^2 = 0.8896 \quad (\text{B146a})$$

$$p_{107} = -0.3136(m_2/m_0) + 2038.7 \quad (\text{B147})$$

$$R_{p_{107}}^2 = 0.9991 \quad (\text{B147a})$$

$$p_{108} = -0.1229(m_2/m_0)^2 + 0.1131(m_2/m_0) + 2045.7 \quad (\text{B148})$$

$$R_{p_{108}}^2 = 0.9913 \quad (\text{B148a})$$

For the additional simulations sub-study (Reading 2033 conditions, unadapted pentahedral boundary-layer grid, case #3) at the inlet bump region:

$$p_{601} = -8.9705(m_2/m_0) + 2069.2 \quad (\text{B149})$$

$$R_{p_{601}}^2 = 0.9999 \quad (\text{B149a})$$

$$p_{602} = -9.7664(m_2/m_0) + 2086.6 \quad (\text{B150})$$

$$R_{p_{602}}^2 = 0.9999 \quad (\text{B150a})$$

$$p_{603} = -13.146(m_2/m_0) + 2093.8 \quad (\text{B151})$$

$$R_{p_{603}}^2 = 0.9999 \quad (\text{B151a})$$

$$p_{604} = -19.961(m_2/m_0) + 2098.9 \quad (\text{B152})$$

$$R_{p_{604}}^2 = 0.9997 \quad (\text{B152a})$$

$$p_{605} = -32.861(m_2/m_0) + 2111 \quad (\text{B153})$$

$$R_{p_{605}}^2 = 0.9994 \quad (\text{B153a})$$

$$p_{606} = -60.631(m_2/m_0) + 2141 \quad (\text{B154})$$

$$R_{p_{606}}^2 = 0.9987 \quad (\text{B154a})$$

$$p_{607} = -133.47(m_2/m_0) + 2224.3 \quad (\text{B155})$$

$$R_{p_{607}}^2 = 0.9968 \quad (\text{B155a})$$

$$p_{608} = -316.85(m_2/m_0)^2 + 704.6(m_2/m_0) + 1597.9 \quad (\text{B156})$$

$$R_{p_{608}}^2 = 0.9997 \quad (\text{B156a})$$

Appendix C.—Statistics

Tables C1 to C27 summarize the average and two times the standard deviation values from the paired t-tests. Note that the paired t-tests utilized the differences between the two data sets that were being compared as the input values.

TABLE C1.—CFD SOLUTIONS ON THE UNADAPTED PENTAHEDRAL BOUNDARY-LAYER GRID COMPARED TO EXPERIMENTAL DATA AT THE READING 1755 CONDITION (INLET DISTORTION)

	Average	2 σ
DPCP	0.042	0.010
DPRP	−0.017	0.006

TABLE C2.—CFD SOLUTIONS ON THE UNADAPTED TETRAHEDRAL BOUNDARY-LAYER GRID COMPARED TO EXPERIMENTAL DATA AT THE READING 1755 CONDITION (INLET DISTORTION)

	Average	2 σ
DPCP	0.005	0.023
DPRP	−0.016	0.008

TABLE C3.—CFD SOLUTIONS ON THE UNADAPTED PENTAHEDRAL BOUNDARY-LAYER SMOOTH GRID COMPARED TO EXPERIMENTAL DATA AT THE READING 1755 CONDITION (INLET DISTORTION)

	Average	2 σ
DPCP	0.000	0.016
DPRP	−0.012	0.004

TABLE C4.—CFD SOLUTIONS ON THE 8 ADAPTATION CYCLE PENTAHEDRAL BOUNDARY-LAYER GRID COMPARED TO EXPERIMENTAL DATA AT THE READING 1755 CONDITION (INLET DISTORTION)

	Average	2 σ
DPCP	0.060	0.011
DPRP	−0.028	0.009

TABLE C5.—CFD SOLUTIONS ON THE 8 ADAPTATION CYCLE TETRAHEDRAL BOUNDARY-LAYER GRID COMPARED TO EXPERIMENTAL DATA AT THE READING 1755 CONDITION (INLET DISTORTION)

	Average	2 σ
DPCP	0.062	0.015
DPRP	−0.020	0.020

TABLE C6.—CFD SOLUTIONS ON THE UNADAPTED TETRAHEDRAL BOUNDARY-LAYER GRID COMPARED TO CFD SOLUTIONS ON THE UNADAPTED PENTAHEDRAL BOUNDARY-LAYER GRID AT THE READING 1755 CONDITION (INLET DISTORTION)

	Average	2 σ
DPCP	−0.037	0.030
DPRP	0.002	0.004

TABLE C7.—CFD SOLUTIONS ON THE UNADAPTED PENTAHEDRAL BOUNDARY-LAYER SMOOTH GRID COMPARED TO CFD SOLUTIONS ON THE UNADAPTED PENTAHEDRAL BOUNDARY-LAYER GRID AT THE READING 1755 CONDITION (INLET DISTORTION)

	Average	2 σ
DPCP	−0.042	0.016
DPRP	0.005	0.003

TABLE C8.—CFD SOLUTIONS ON THE 8 ADAPTATION CYCLE PENTAHEDRAL BOUNDARY-LAYER GRID COMPARED TO CFD SOLUTIONS ON THE UNADAPTED PENTAHEDRAL BOUNDARY-LAYER GRID AT THE READING 1755 CONDITION (INLET DISTORTION)

	Average	2 σ
DPCP	0.018	0.009
DPRP	−0.011	0.004

TABLE C9.—CFD SOLUTIONS ON THE 8 ADAPTATION CYCLE TETRAHEDRAL BOUNDARY-LAYER GRID COMPARED TO CFD SOLUTIONS ON THE UNADAPTED PENTAHEDRAL BOUNDARY-LAYER GRID AT THE READING 1755 CONDITION (INLET DISTORTION)

	Average	2 σ
DPCP	0.020	0.013
DPRP	−0.003	0.015

TABLE C10.—CFD SOLUTIONS ON THE UNADAPTED PENTAHEDRAL BOUNDARY-LAYER SMOOTH GRID COMPARED TO CFD SOLUTIONS ON THE UNADAPTED TETRAHEDRAL BOUNDARY-LAYER GRID AT THE READING 1755 CONDITION (INLET DISTORTION)

	Average	2 σ
DPCP	−0.004	0.023
DPRP	0.003	0.005

TABLE C11.—CFD SOLUTIONS ON THE 8 ADAPTATION CYCLE PENTAHEDRAL BOUNDARY-LAYER GRID COMPARED TO CFD SOLUTIONS ON THE UNADAPTED TETRAHEDRAL BOUNDARY-LAYER GRID AT THE READING 1755 CONDITION (INLET DISTORTION)

	Average	2 σ
DPCP	0.055	0.034
DPRP	−0.013	0.006

TABLE C12.—CFD SOLUTIONS ON THE 8 ADAPTATION CYCLE TETRAHEDRAL BOUNDARY-LAYER GRID COMPARED TO CFD SOLUTIONS ON THE UNADAPTED TETRAHEDRAL BOUNDARY-LAYER GRID AT THE READING 1755 CONDITION (INLET DISTORTION)

	Average	2 σ
DPCP	0.057	0.038
DPRP	−0.005	0.012

TABLE C13.—CFD SOLUTIONS ON THE 8 ADAPTATION CYCLE PENTAHEDRAL BOUNDARY-LAYER GRID COMPARED TO CFD SOLUTIONS ON THE UNADAPTED PENTAHEDRAL BOUNDARY-LAYER SMOOTH GRID AT THE READING 1755 CONDITION (INLET DISTORTION)

	Average	2 σ
DPCP	0.060	0.023
DPRP	-0.016	0.007

TABLE C14.—CFD SOLUTIONS ON THE 8 ADAPTATION CYCLE TETRAHEDRAL BOUNDARY-LAYER GRID COMPARED TO CFD SOLUTIONS ON THE UNADAPTED PENTAHEDRAL BOUNDARY-LAYER SMOOTH GRID AT THE READING 1755 CONDITION (INLET DISTORTION)

	Average	2 σ
DPCP	0.062	0.027
DPRP	-0.008	0.017

TABLE C15.—CFD SOLUTIONS ON THE 8 ADAPTATION CYCLE TETRAHEDRAL BOUNDARY-LAYER GRID COMPARED TO CFD SOLUTIONS ON THE 8 ADAPTATION CYCLE PENTAHEDRAL BOUNDARY-LAYER GRID AT THE READING 1755 CONDITION (INLET DISTORTION)

	Average	2 σ
DPCP	0.002	0.005
DPRP	0.008	0.013

TABLE C16.—CFD SOLUTIONS ON THE UNADAPTED PENTAHEDRAL BOUNDARY-LAYER GRID COMPARED TO EXPERIMENTAL DATA AT THE READING 1771 CONDITION (CAMERA FAIRING PRESSURE MEASUREMENTS)

	Average, psf	2 σ , psf
P101	1.886	2.944
P102	2.368	2.504
P103	3.015	1.175
P104	12.955	0.923
P105	-1.439	1.456
P106	-18.432	1.281
P107	3.671	2.554
P108	3.445	1.951

TABLE C17.—CFD SOLUTIONS ON THE UNADAPTED PENTAHEDRAL BOUNDARY-LAYER GRID COMPARED TO EXPERIMENTAL DATA AT THE READING 1771 CONDITION (INLET BUMP PRESSURE MEASUREMENTS)

	Average, psf	2 σ , psf
P601	-5.298	0.856
P602	-1.561	1.520
P603	-1.591	1.772
P604	-2.954	0.829
P605	-3.854	4.697
P606	-3.469	32.329
P607	-2.334	51.566
P608	-1.588	28.174

TABLE C18.—CFD SOLUTIONS ON THE UNADAPTED TETRAHEDRAL
BOUNDARY-LAYER GRID COMPARED TO EXPERIMENTAL DATA
AT THE READING 1771 CONDITION (CAMERA FAIRING
PRESSURE MEASUREMENTS)

	Average, psf	2 σ , psf
P101	3.309	2.942
P102	2.733	2.503
P103	2.700	1.172
P104	15.266	0.928
P105	1.688	1.454
P106	NA	NA
P107	1.594	2.554
P108	-0.202	1.9509

TABLE C19.—CFD SOLUTIONS ON THE UNADAPTED TETRAHEDRAL
BOUNDARY-LAYER GRID COMPARED TO EXPERIMENTAL DATA
AT THE READING 1771 CONDITION (INLET BUMP
PRESSURE MEASUREMENTS)

	Average, psf	2 σ , psf
P601	-5.137	0.853
P602	-1.753	1.443
P603	-1.684	1.532
P604	-3.054	1.001
P605	-3.082	1.585
P606	-3.500	30.932
P607	-2.281	25.535
P608	-2.393	30.281

TABLE C20.—CFD SOLUTIONS ON THE UNADAPTED PENTAHEDRAL
BOUNDARY-LAYER GRID COMPARED TO CFD SOLUTIONS ON
THE UNADAPTED TETRAHEDRAL BOUNDARY-LAYER GRID
AT THE READING 1771 CONDITION (CAMERA FAIRING
PRESSURE MEASUREMENTS)

	Average, psf	2 σ , psf
P101	-1.423	0.002
P102	-0.365	0.002
P103	0.315	0.013
P104	-2.311	0.015
P105	-3.127	0.004
P106	NA	NA
P107	1.851	0.002
P108	0.0557	0.000

TABLE C21.—CFD SOLUTIONS ON THE UNADAPTED PENTAHEDRAL
BOUNDARY-LAYER GRID COMPARED TO CFD SOLUTIONS ON
THE UNADAPTED TETRAHEDRAL BOUNDARY-LAYER GRID
AT THE READING 1771 CONDITION (INLET BUMP
PRESSURE MEASUREMENTS)

	Average, psf	2 σ , psf
P601	-0.161	0.016
P602	0.193	0.153
P603	0.093	0.509
P604	0.100	0.716
P605	-0.051	4.390
P606	0.030	1.902
P607	-0.053	45.980
P608	0.805	2.627

TABLE C22.—CFD SOLUTIONS ON THE UNADAPTED PENTAHEDRAL
BOUNDARY-LAYER GRID COMPARED TO EXPERIMENTAL DATA
AT THE READING 2033 CONDITION (CAMERA FAIRING
PRESSURE MEASUREMENTS)

	Average, psf	2 σ , psf
P101	1.868	0.678
P102	2.376	0.761
P103	2.983	0.690
P104	13.021	0.937
P105	-1.406	0.710
P106	3.648	0.712
P107	3.404	0.743
P108	0.352	0.752

TABLE C23.—CFD SOLUTIONS ON THE UNADAPTED PENTAHEDRAL
BOUNDARY-LAYER GRID COMPARED TO EXPERIMENTAL DATA
AT THE READING 2033 CONDITION (INLET BUMP
PRESSURE MEASUREMENTS)

	Average, psf	2 σ , psf
P601	-5.427	0.715
P602	-1.658	0.676
P603	-1.658	0.716
P604	-3.104	0.735
P605	-4.098	0.874
P606	-3.789	1.079
P607	-2.802	2.067
P608	-5.432	7.813

TABLE C24.—CFD SOLUTIONS ON THE UNADAPTED TETRAHEDRAL
BOUNDARY-LAYER GRID COMPARED TO EXPERIMENTAL DATA
AT THE READING 2033 CONDITION (CAMERA FAIRING
PRESSURE MEASUREMENTS)

	Average, psf	2 σ , psf
P101	1.876	0.711
P102	2.702	0.760
P103	2.718	0.683
P104	15.220	0.939
P105	1.664	0.731
P106	1.730	19.063
P107	1.508	0.739
P108	-0.175	0.746

TABLE C25.—CFD SOLUTIONS ON THE UNADAPTED TETRAHEDRAL
BOUNDARY-LAYER GRID COMPARED TO EXPERIMENTAL DATA
AT THE READING 2033 CONDITION (INLET BUMP
PRESSURE MEASUREMENTS)

	Average, psf	2 σ , psf
P601	-5.120	0.717
P602	-1.775	0.675
P603	-1.674	0.715
P604	-3.075	0.735
P605	-3.965	0.889
P606	-3.579	1.091
P607	-2.364	2.056
P608	-4.514	7.770

TABLE C26.—CFD SOLUTIONS ON THE UNADAPTED PENTAHEDRAL
BOUNDARY-LAYER GRID COMPARED TO CFD SOLUTIONS ON
THE UNADAPTED TETRAHEDRAL BOUNDARY-LAYER GRID
AT THE READING 2033 CONDITION (CAMERA FAIRING
PRESSURE MEASUREMENTS)

	Average, psf	2 σ , psf
P101	−0.008	0.415
P102	−0.326	0.003
P103	0.265	0.034
P104	−2.199	0.008
P105	−3.070	0.057
P106	1.942	18.915
P107	1.896	0.014
P108	0.527	0.027

TABLE C27.—CFD SOLUTIONS ON THE UNADAPTED PENTAHEDRAL
BOUNDARY-LAYER GRID COMPARED TO CFD SOLUTIONS ON
THE UNADAPTED TETRAHEDRAL BOUNDARY-LAYER GRID
AT THE READING 2033 CONDITION (INLET BUMP
PRESSURE MEASUREMENTS)

	Average, psf	2 σ , psf
P601	−0.307	0.006
P602	0.117	0.001
P603	0.016	0.001
P604	−0.029	3.72×10^{-13}
P605	−0.133	0.023
P606	−0.210	0.020
P607	−0.438	0.071
P608	−0.918	0.189

References

1. Broge, J.L., “Aerion Progresses on the AS2 with Help from Airbus, and Announces First Fleet Customer,” SAE International, URL: <http://articles.sae.org/14491/> [cited 30 March 2018].
2. McMillin, M., “Spike Aerospace Enlarges Supersonic Jet Development Effort,” *The Weekly Business of Aviation*, 26 Jan. 2017, pp. 4.
3. Norris, G., “Baby Boom’ Supersonic Demonstrator Unveiled,” *Aviation Daily*, 15 Nov. 2016, pp. 3.
4. Civil Aircraft Sonic Boom, 14 C.F.R. § 91.817 2017.
5. “NASA Aeronautics Strategic Implementation Plan 2017 Update,” NASA Aeronautics Strategic Implementation Plan, URL: <https://www.nasa.gov/sites/default/files/atoms/files/sip-2017-03-23-17-high.pdf> [cited 1 May 2018].
6. “New Aviation Horizons Initiative and Complementary Investments,” NASA, URL: <https://www.nasa.gov/sites/default/files/atoms/files/nasa-aero-10-yr-plan-508-reduced.pdf> [cited 1 May 2018].
7. Warwick, G., “Affordable Low-Boom X-Plane Goal of Lockheed’s QueSST Design,” *Aviation Week & Space Technology*, 3 March 2016, pp. 21.
8. Biedron, R.T., et al., “FUN3D Manual: 13.1,” NASA/TM—2017-219580, February 2017.
9. Park, M.A., and Carlson, J.-R., “Turbulent Output-Based Anisotropic Adaptation,” AIAA–2010–0168, January 2010.
10. Alkandry, H., Park, M.A., Kleb, W.L., and Boyd, I.D., “Feature-Based and Output-Based Grid Adaptation Study for Hypersonic Propulsive Deceleration Jet Flows,” October 2010.
11. Bartels, R.E., Vatsa, V., Carlson, J.-R., Park, M., and Mineck, R.E., “FUN3D grid Refinement and Adaptation Studies for the Ares Launch Vehicle,” AIAA–2010–4372, June 2010.
12. Park, M.A., and Darmofal, D.L., “Validation of an Output-Adaptive, Tetrahedral Cut-Cell Method for Sonic Boom Prediction,” *AIAA Journal*, vol. 48, no. 9, 2010, pp. 1928–1945.
13. Davis, Z.S., and Park, M.A., “IFCPT S-Duct Grid-Adapted FUN3D Computations for the Third Propulsion Aerodynamics Workshop,” AIAA–2017–4835, July 2017.
14. Pointwise, Software Package, Version 17.3 Release 4, Pointwise Inc., Fort Worth, TX, 2015.
15. AFLR3, Software Package, Version 15.5.5, CAVS Sim Center, Mississippi State University, Starkville, MS, 2015.
16. Marcum, D.L., and Weatherill, N.P., “Unstructured Grid Generation Using Iterative Point Insertion and Local Reconstruction,” *AIAA Journal*, vol. 33, no. 9, 1995, pp. 1619–1625.
17. Marcum, D.L., “Unstructured Grid Generation Using Automatic Point Insertion and Local Reconstruction,” *The Handbook of Grid Generation*, edited by J.F. Thompson, B. Soni, and N.P. Weatherill, CRC Press, 1998, pp. 18–1 through 18–31.
18. Spalart, P., and Allmaras, S., “A One-Equation Turbulence Model for Aerodynamic Flows,” *La Recherche Aeronautique*, no. 1, 1984, pp. 5–21.
19. Society of Automotive Engineers Inc., “Gas Turbine Engine Inlet Flow Distortion Guidelines,” ARP 1420 Rev. B, 2011.
20. Venditti, D.A., “Grid Adaptation for Functional Outputs of Compressible Flow Simulations,” PhD thesis, Massachusetts Institute of Technology, Cambridge, MA, 2002.

